J. Fluid Mech. (1998), *vol.* 371, *pp.* 233–268. Printed in the United Kingdom

Miscible porous media displacements in the quarter five-spot configuration. Part 1. The homogeneous case

By CHING-YAO CHEN AND ECKART MEIBURG

Department of Aerospace Engineering, University of Southern California, Los Angeles, CA 90089-1191, USA

(Received 19 November 1997 and in revised form 7 May 1998)

A detailed two-part computational investigation is conducted into the dynamical evolution of two-dimensional miscible porous media flows in the quarter five-spot arrangement of injection and production wells. High-accuary direct numerical simulations are performed that reproduce all dynamically relevant length scales in solving the vorticity–streamfunction formulation of Darcy's law. The accuracy of the method is demonstrated by a comparison of simulation data with linear stability results for radial source flow.

Within this part, Part 1 of the present investigation, a series of simulations is discussed that demonstrate how the mobility ratio and the dimensionless flow rate denoted by the Péclet number Pe affect both local and integral features of homogeneous displacement processes. Mobility ratios up to 150 and Pe-values up to 2000 are investigated. For sufficiently large Pe-values, the flow near the injection well gives rise to a vigorous viscous fingering instability. As the unstable concentration front approaches the central region of the domain, nonlinear interactions between the fingers similar to those known from unidirectional flows are observed, such as merging, partial merging, and shielding, along with secondary tip-splitting and side-branching instabilities. At large Pe-values, several of these fingers compete for long times, before one of them accelerates ahead of the others and leads to the breakthrough of the front.

In contrast to unidirectional flows, the quarter five-spot geometry imposes both an external length scale and a time scale on the flow. The resulting spatial non-uniformity of the potential base flow is observed to lead to a clear separation in space and time of large and small scales in the flow. Small scales occur predominantly during the early stages near the injection well, and at late times near the production well. The central domain is dominated by larger scales.

Taken together, the results of the simulations demonstrate that both the mobility ratio and Pe strongly affect the dynamics of the flow. While some integral measures, such as the recovery at breakthrough, may show only a weak dependence on Pe for large Pe-values, the local fingering dynamics continue to change with Pe.

The increased susceptibility of the flow to perturbations during the early stages provides the motivation to formulate an optimization problem that attempts to maximize recovery, for a constant overall process time, by employing a time-dependent flow rate. Within the present framework, which accounts for molecular diffusion but not for velocity-dependent dispersion, simulation results indeed indicate the potential to increase recovery by reducing the flow rate at early times, and then increasing it during the later stages.

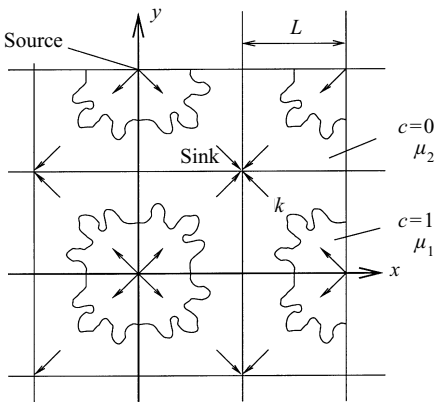

FIGURE 1. The quarter five-spot configuration of injection and production wells.

1. Introduction

Accurate predictive capabilities for displacements in porous media represent a prerequisite for addressing a host of problems in fields such as hydrology or enhanced oil recovery. Traditionally, most of the analytical, experimental and numerical investigations in this area have been performed for unidirectional flows, cf. the recent review articles by Homsy (1987) and Yortsos (1990). However, localized injection and production wells, present in most applications, can significantly alter the overall dynamics of the displacement processes. Due to its practical importance in enhanced oil recovery, the quarter five-spot arrangement of injection and production wells (figure 1) has served as the paradigm configuration for exploring these effects. Spanning four decades, investigations of quarter five-spot flows have focused both on miscible and on immiscible displacements, in homogeneous as well as heterogeneous porous media. The main objective lies in the exploration of the governing physical mechanisms and the interactions among them, in order to gain an understanding of the dynamics at a level that is fundamental enough to aid in the development of more accurate models, which in turn should allow improved performance predictions of large reservoirs. In the present investigation, we pursue this goal by means of highly accurate direct numerical simulations, which resolve the entire spectrum of length scales without introducing significant levels of numerical diffusion.

The early experiments by Habermann (1960) have demonstrated how, for an unfavourable mobility ratio, the development of viscous fingers lowers the recovery at breakthrough of quarter five-spot flows. Further early measurements for this geometry are reported by Simmons *et al.* (1959), Caudle & Witte (1959), and Lacey, Faris & Brinkman (1961). The observed unstable fingering is similar to findings in rectilinear displacements, exemplified by the investigations of Slobod & Thomas (1963), Perkins, Johnston & Hoffman (1965), and Wooding (1969). While it was recognized that this behaviour is qualitatively related to the instability mechanism described by Hill (1952), Saffman & Taylor (1958), and Chouke, van Meurs & van der Poel (1959) for a unidirectional flow, the more complex quarter five-spot geometry posed a harder problem for quantifying the nature of the instability. The main reason lies in the absence of exact solutions for variable-viscosity quarter five-spot flows, which could serve as steady or quasi-steady base states for a linear stability analysis. In addition, there is a lack of understanding of the mechanisms that determine the characteristic scales of the nonlinearly evolving fingers, and the

dynamical interactions among them. The goal of the present investigation thus is to gain insight into the unsteady development of quarter five-spot flows as a function of the relevant governing parameters, in particular the mobility ratio, the dimensionless flow rate, and, in Part 2 (Chen & Meiburg 1998), the correlation lengths and variance of permeability heterogeneities.

An important step towards understanding the dynamics of homogeneous quarter five-spot flows lies in the realization that in the neighbourhood of the injection well the flow is nearly radially symmetric. The stability investigations by Tan & Homsy (1987) and Yortsos (1987) for radial two-phase flows should hence aid in understanding the nature of the fingering instability and its role during the early stages of miscible quarter five-spot flows. Their analysis demonstrates that the instability grows algebraically in radial source flows, as opposed to the exponential growth observed in rectilinear flows. Growth rates, wavenumbers of maximum growth, and short-wave cutoff wavenumbers are all determined by the mobility ratio and the dimensionless injection rate in the form of a Péclet number.

As far as the nonlinear evolution of homogeneous quarter five-spot flows is concerned, some guidance can be obtained from simulations of rectilinear flows. Efforts in this area date back at least to the work by Peaceman & Rachford (1962), who developed a finite difference algorithm for computing an unstable rectilinear miscible displacement. A large amount of detailed information is provided by the more recent high-accuracy time-dependent simulations of Tan & Homsy (1988). These authors formulate the miscible fingering problem in terms of vorticity and streamfunction variables, an approach that had already proved useful in earlier immiscible fingering calculations, e.g. Tryggvason & Aref (1983) and Meiburg & Homsy (1988). Using a Fourier spectral method, Tan & Homsy explore miscible viscous fingering dynamics as a function of the mobility ratio and the Péclet number. During the initial development, the authors find good agreement with the growth rates of their earlier linear stability investigation (Tan & Homsy 1986). As their amplitudes grow, the fingers evolve and interact through complex dynamical processes involving spreading, shielding, and splitting. These nonlinear mechanisms, which can best be understood in terms of the underlying vorticity dynamics, dominate the evolution of the characteristic global scales of the flow. One such scale is the one-dimensional mixing length, which initially grows like the square root of time, to be followed by linear growth during the later stages; an observation that is confirmed by the investigation of Bacri *et al.* (1992). The finite difference simulations of unidirectional displacements by Christie & Bond (1987) and Christie (1989) exhibit similar fingering dynamics and yield good global quantitative agreement with the experimental recovery data of Blackwell, Rayne & Terry (1959). Several other computational investigators, e.g. Sherwood (1987), Fayers, Blunt & Christie (1992) and Bratvedt *et al.* (1992), choose not to account for molecular diffusion or dispersion, so that the computational grid has to provide the short-wavelength cutoff via numerical diffusion. Even though this approach produces fingering as well, it is not suitable for a detailed direct numerical investigation of miscible displacements, as the simulation results depend on the numerical discretization. More recently, Blunt and coworkers (Batycky, Blunt & Thiele 1996; Thiele *et al.* 1996) utilize mapping of numerical solutions along streamlines in order to simulate three-dimensional miscible displacements in heterogeneous five-spot configurations. Their simulations, which take into account gravitational forces as well, exhibit vigorous viscous fingering. The method furthermore allows big improvements in efficiency, although in the absence of physical diffusion or dispersion, numerical diffusion sets the short-wave cutoff length scale and hence may have a substantial effect on the

results. King & Scher (1985) as well as Araktingi & Orr (1988) employ a probabilistic numerical scheme, based on a random walk model, in order to explore stability issues and the transition from fingering-dominated displacements to those dominated by heterogeneity effects in the rectilinear configuration. A more complete review of computational approaches to porous media flows is provided by Meiburg & Chen (1997).

Rogerson & Meiburg (1993*a*) extend the original stability investigation by Tan & Homsy (1986) for unidirectional displacements to two-dimensional base flows involving shear across the interface. They observe a stabilization of the front by the shear, which affects both the growth rate and the preferred wavelength of the instabiliy. Numerical simulations by the same authors (Rogerson & Meiburg 1993*b*) confirm this stabilization. They furthermore exhibit new nonlinear fingering mechanisms as well, among them a secondary side-finger instability, which alter the global one-dimensional measures of the displacement process.

In terms of understanding and quantifying the governing physical mechanisms and the interactions among them, the quarter five-spot geometry poses a somewhat more challenging problem than unidirectional flow, both physically and computationally. The irrotational, constant mobility flow field now gives rise to a spatially varying strain field, which will stretch and compress the concentration front, thereby affecting the stability of the flow. Furthermore, in contrast to unidirectional flows, the quarter five-spot flow imposes externally prescribed length and time scales on the problem. In addition, computationally the quarter five-spot flow is harder to treat than the rectilinear flow as well. First of all, the velocity field becomes singular near the injection and production wells, so that the velocity magnitude can vary by several orders of magnitude throughout the flow field. This singular behaviour adversely affects the accuracy of the numerical differentiation, in particular near the injection and production wells. Interestingly, this problem becomes more significant for finer computational grids, which locate mesh points closer to the singular corners. The CFL condition on the time step renders explicit schemes less desirable for quarter five-spot flows. In addition, the non-periodic boundaries limit the use of highly accurate Fourier-based spectral methods, such as the one employed by Homsy and coworkers. Nevertheless, there have been a few numerical investigations that have shed some light onto miscible quarter five-spot flows. Christie (1989) presents a finite-difference-based simulation of the quarter five-spot flow in a reservoir with permeability heterogeneities. He employs an explicit flux-corrected transport method (FCT, Christie & Bond 1985) with first-order time accuracy on a 150×150 grid. While the simulation shows a vigorous fingering instability, the author points out that the dynamics of the evolving fingers is affected by the orientation of the computational grid. Ewing, Russel & Young (1989) performed finite element simulations for anisotropic, heterogeneous, miscible flows in the quarter five-spot geometry, using grids up to 100×100. The authors typically observe a dominance of the viscous fingering instability over permeability related effects. In general, the relative importance of these effects is, of course, expected to depend on the viscosity ratio and the degree of heterogeneity of the porous medium. The simulations allow the authors to draw a variety of conclusions about the importance of both anisotropy and heterogeneity. At the same time, they state a number of issues left unresolved by their work, thereby emphasizing the need for further, higher accuracy simulations. None of the above investigations attempts to systematically evaluate the effect of the mobility ratio and the dimensionless flow rate on the overall dynamics of the displacement process.

A more recent investigation by Zhang, Sorbie & Tsibuklis (1997) analyses the quarter five-spot flow both experimentally and numerically, for different values of the

mobility ratio. The computational method is again based on finite differences, and it has second-order accuracy in space and time. As the authors point out, in spite of a large value of the Péclet number the simulations do not exhibit the fine-scale structure seen in the experiments. This, along with the fact that fingering had to be triggered by artificial permeability inhomogeneities, suggests that numerical diffusion may have had some effect on the computational results. While the authors do not attempt to evaluate the influence of molecular diffusion, their results regarding overall recovery and sweep efficiency show good agreement with the experimental measurements.

The above observations indicate that lower-order methods often do not allow the accurate and detailed representation of complex physical mechanisms, due to the large amounts of numerical diffusion and dispersion they introduce. Nevertheless, for some situations they achieve good agreement with certain integral quantities obtained from experiments, such as overall recovery or sweep efficiency. While this merely reflects the insensitivity of some global quantities to the levels of these numerical artifacts, it should not obscure the fact that the in-depth understanding needed for designing and evaluating improved oil recovery methods requires high accuracy simulations. Especially for applications involving large Péclet numbers, it is imperative that numerical diffusion and dispersion be kept to a minimum, as they alter both the growth rate and the length scales of the fingering instability. In fact, when the computational algorithm introduces excessive numerical diffusion, the growth of fingers can be suppressed altogether. This represents the reason why in many earlier investigations fingers had to be triggered explicitly by permeability heterogeneities. Thus there is a clear need for developing efficient computational techniques that can accurately simulate the detailed dynamics of multiphase porous media flows in complex geometries, without giving rise to significant numerical errors. For rectilinear flows, the Fourier-based spectral method by Tan & Homsy (1988) shows excellent accuracy, as does the Chebyshev collocation method introduced by Hatziavramidis (1990). Tchelepi *et al.* (1993) and Tchelepi & Orr (1994) minimize the amount of numerical diffusion by employing a particle tracking technique, although the solution of the accompanying pressure equation still results in some artificial smoothing. Other authors, e.g. Paterson (1984) and DeGregoria (1985) employ a diffusion-limited aggregation approach. However, the stochastic nature of this approach prevents the accurate simulation of the small-scale dynamics.

The present investigation employs a novel and highly accurate numerical approach recently developed by the present authors for direct numerical simulations of miscible porous media flows (Meiburg & Chen 1997). The numerical method is designed to handle geometries that are more demanding than the standard unidirectional case, and it has been validated and tested for the quarter five-spot configuration. While its formal accuracy is fourth order in space and second order in time, diffusive terms are represented with sixth-order accuracy. It is based on compact high-order finite differences (Lele 1992) and has the flexibility to handle non-periodic, complex boundaries.

The outline of this part, Part 1 of the present investigation, is as follows. After formulating the physical problem in §2, the computational technique will briefly be reviewed in §3. Subsequently, computational results regarding the effects of both the dimensionless flow rate and the mobility ratio will be presented in §4. Here, the emphasis will be on analysing the detailed unsteady dynamics, as well as its effect on the global measures of the displacement process. Furthermore, the question will be addressed as to whether a time-dependent injection protocol can increase the overall recovery. Finally, §5 will discuss and compare the current results in light of earlier experimental and numerical findings. In Part 2 (Chen & Meiburg 1998), the effect

of permeability variations, characterized by a given variance and correlation length, will be analysed in detail, while Part 3 (Pankiewitz & Meiburg 1998) will address the effects of non-monotonic viscosity profiles in miscible quarter five-spot displacements.

The current investigation, as well as most earlier ones, employ a continuum formulation based on Darcy's law. Consequently, it does not address the effects of microscale phenomena related to such issues as pore geometry, capillarity, wetting properties and many more. For a detailed discussion of these and other topics, as well as macroscopic versus microscopic approaches, the reader is referred to the comprehensive review articles by Wooding & Morel-Seytoux (1976), Saffman (1986), Homsy (1987), Adler & Brenner (1988), and Yortsos (1990).

2. Governing equations

The quarter five-spot geometry represents a staggered configuration of production and injection wells of particular practical importance (figure 1). By realizing that the overall geometry is composed of many identical building blocks, and by assuming that the flow is identical in each one of these, we can take one such building block as our computational domain, provided that the proper symmetry boundary conditions are specified along its borders. We are interested in solving for the unstable, time-dependent, incompressible flow generated by a miscible displacement process under Darcy's law

$$\nabla \cdot \boldsymbol{u} = 0, \tag{2.1}$$

$$\nabla p = -\frac{\mu}{k}\boldsymbol{u}, \tag{2.2}$$

$$\frac{\partial c}{\partial t} + \boldsymbol{u} \cdot \nabla c = D\nabla^2 c. \tag{2.3}$$

Our attention focuses on the two-dimensional flow in a horizontal plane, so that gravity does not have an effect. The above equations express the conservation of mass, momentum, and species, with c denoting the concentration of the displacing fluid. As a starting point in our computational investigation, we account only for molecular diffusion, as expressed by a scalar diffusion coefficient D. At a later point, D will be replaced by a more realistic dispersion tensor, in order to account for the effects of flow-related dispersion (Taylor 1953). Here, the formulation of a proper dispersion tensor will have to account for recent findings regarding flow-induced mixing at the pore level, cf. Petitjeans & Maxworthy (1996), Chen & Meiburg (1996), Yang & Yortsos (1997). The stability analysis performed by Yortsos & Zeybek (1988) as well as the nonlinear simulations of Zimmerman & Homsy (1992), both for rectilinear displacements, demonstrate the potential influence that velocity-dependent dispersion can have on the nature of the displacement process.

The viscosity μ is supposed to be a known function of the concentration, and the permeability has a given spatial distribution

$$\mu = \mu(c), \quad k = k(x, y). \tag{2.4}$$

In order to render the governing equations dimensionless, we take the lateral extent L of one unit of the flow field as the characteristic length scale. In conjunction with the source strength per depth $2\pi Q$ we then obtain a time scale as L^2/Q, and a velocity scale in the form of Q/L. The permeability is referred to a characteristic value K. We furthermore scale viscosity, density, and pressure with μ_1, ρ_1, and $Q\mu_1/K$, respectively,

where the subscript 1 indicates the displacing fluid. Along the sides of the domain we require the obvious symmetry boundary conditions

$$x = 0, 1: \; u = 0, \quad v_x = 0, \quad c_x = 0, \quad k_x = 0; \tag{2.5}$$

$$y = 0, 1: \; u_y = 0, \quad v = 0, \quad c_y = 0, \quad k_y = 0. \tag{2.6}$$

These boundary conditions are needed to maintain the symmetry of the flow field, which allows us to reduce the full five-spot problem to that of a quarter five-spot. It should be pointed out that the line connecting the source with the sink diagonally across the quarter five-spot element represents a further line of symmetry. However, we do not enforce this symmetry, so that the flow is free to develop asymmetries within the quarter five-spot element. For the purpose of solving the equations numerically, it is convenient to recast them into the well-known streamfunction–vorticity (ψ, ω) formulation (Tryggvason & Aref 1983; Meiburg & Homsy 1988; Tan & Homsy 1988). By introducing the streamfunction ψ and the vorticity ω in the usual way, the continuity equation is satisfied identically. The set of governing dimensionless equations then takes the form

$$c_t + \psi_y c_x - \psi_x c_y = \frac{1}{Pe} \nabla^2 c, \tag{2.7}$$

$$\omega = \frac{1}{\mu} \frac{\mathrm{d}\mu}{\mathrm{d}c} (\nabla\psi \cdot \nabla c) - \frac{1}{k} \nabla\psi \cdot \nabla k, \tag{2.8}$$

$$\nabla^2 \psi = -\omega, \tag{2.9}$$

where the Péclet number

$$Pe = \frac{Q}{D} \tag{2.10}$$

can be interpreted as a dimensionless flow rate. Following other researchers (e.g. Tan & Homsy 1986; Rogerson & Meiburg 1993*a*,*b*), we define

$$R = -\frac{1}{\mu} \frac{\mathrm{d}\mu}{\mathrm{d}c} \tag{2.11}$$

and consider R to be a constant for a given combination of fluids. In this way, the viscosity dependence on the concentration has the form

$$\mu(c) = e^{R(1-c)}. \tag{2.12}$$

Alternatively, other viscosity-concentration relationships, such as for example the quarter power law, could easily be implemented as well. One computational difficulty arises from the fact that the flow has singularities at both well locations, making accurate computations difficult due to problems related to numerical differentiation near these locations. Our approach to overcoming this obstacle is based on a splitting of the solution into a potential component $\boldsymbol{u}_{pot}(\boldsymbol{x})$ that absorbs the wells, plus a rotational part $\boldsymbol{u}_{rot}(\boldsymbol{x})$ which is smooth and can be obtained with high accuracy via the above mentioned compact finite difference approach. The potential part of the flow consists of a two-dimensional staggered array of point sources and sinks arranged in the quarter five-spot configuration. The corresponding velocity field can either be evaluated on the basis of the results provided by Morel-Seytoux (1965, 1966, cf. also Muskat 1937), or approximate analytical expressions can be constructed to any desired accuracy by superimposing the well-known results for rows of point sources and sinks, cf. Lamb (1932), Meiburg & Chen (1997). In order to avoid numerical instabilities,

we furthermore smooth out the point sources and sinks by distributing their strength in a Gaussian way, typically over a radius of about 0.05. Consequently, by using these analytically available expressions for the potential component of the streamfunction ψ_{pot} and its derivatives, inaccuracies related to the existence of the singularities can be greatly reduced, yielding a much more accurate representation of the flow near the injection and production wells. Furthermore, the closed-form solution of the potential flow component will aid in eliminating grid orientation effects, cf. also the discussion below (Christie & Bond 1987; Christie 1989; Brand, Heineman & Aziz 1991). Since the Laplacian of the potential streamfunction component vanishes, our governing equations and boundary conditions become

$$c_t + \psi_y c_x - \psi_x c_y = \frac{1}{Pe}\nabla^2 c, \tag{2.13}$$

$$\omega = -R\,(\nabla\psi \cdot \nabla c) - \frac{1}{k}\nabla\psi \cdot \nabla k, \tag{2.14}$$

$$\nabla^2 \psi_{rot} = -\omega, \tag{2.15}$$

$$\psi = \psi_{pot} + \psi_{rot}, \tag{2.16}$$

where ψ_{rot} is the rotational component of the streamfunction. The symmetry boundary conditions at the sides now are

$$x = 0, 1\text{:}\ \ c_x = 0, \quad \omega = 0, \quad \psi_{rot} = 0, \quad k_x = 0, \tag{2.17}$$

$$y = 0, 1\text{:}\ \ c_y = 0, \quad \omega = 0, \quad \psi_{rot} = 0, \quad k_y = 0. \tag{2.18}$$

Suitable initial conditions can be specified, for example, as

$$\psi(\boldsymbol{x}, t = t_i) = \psi_{pot}(\boldsymbol{x}), \tag{2.19}$$

$$c(\boldsymbol{x}, t = t_i) = c_0(\boldsymbol{x}). \tag{2.20}$$

In the present simulations, we take $c_0(\boldsymbol{x})$ from the one-dimensional similarity solutions provided by Tan & Homsy (1987) as well as Yortsos (1987) for radial source flow at time t_i. The starting time t_i of the simulation is taken to be non-zero, in order to avoid a singular initial concentration profile. The influence of t_i on the simulation results will be discussed below. Since this part of the present investigation addresses homogeneous flows only, k is unity throughout the entire domain.

3. Numerical technique

For the reasons mentioned ealier, the solution procedure for the governing equations will be based on high-order compact finite difference approximations. In the following, only a brief outline of the computational method will be provided. Details, as well as a more complete review of the literature on numerical techniques in reservoir simulation, can be found in Chen (1998) as well as Meiburg & Chen (1997). As for the time-stepping scheme, the traditional use of explicit methods, applied for example by Tan & Homsy (1988) for rectilinear displacements, has considerable drawbacks for the quarter five-spot flow. The reason lies in the singularities at the well locations, near which the fluid velocities are orders of magnitude larger than in the centre of the domain. For example, on a 1024^2 grid for a two-dimensional simulation, which represents the finest discretization employed within the present investigation, the magnitude of the velocities will vary by $O(10^3)$ between the grid points nearest to the

wells and those at the centre of the computational domain. For explicit schemes, these small regions near the wells consequently determine the maximum allowable time step as a result of stability restrictions in terms of a CFL number. For this reason, we solve the concentration equation implicitly by means of the Alternating-Direction-Implicit (ADI) approach (Peaceman & Rachford 1955), cf. Meiburg & Chen (1997). Our ADI procedure, of second-order accuracy in time, advances the concentration field over a full time step by carrying out two successive half-steps. During the first one of these, the convection and diffusion terms in the x-direction are treated implicitly, while those in the y-direction are dealt with explicitly. During the second half-step, the roles are reversed, so that now the y-direction is implicit while the x-direction is explicit. The convection terms are discretized with fourth-order accuracy when implicit, and with sixth-order accuracy when explicit. Diffusive terms are always discretized with sixth-order accuracy, as is the right-hand side of the vorticity equation.

The elliptic Poisson equation for the determination of the rotational component of the streamfunction from the vorticity distribution can be solved efficiently on the basis of fast Fourier transform methods (Gottlieb & Orszag 1977). We found that for large values of R and Pe, a few underrelaxed iterations between the vorticity and the streamfunction equations became necessary in order to obtain convergence. This might possibly represent the reason for the numerical instability observed by Tan & Homsy (1988) at large values of these parameters. After obtaining the streamfunction, the velocity components are computed by differentiation in Fourier space.

3.1. *Validation*

Rigorous validation represents an important step in establishing the accuracy and convergence properties of a novel numerical approach. As discussed in detail in Meiburg & Chen (1997), we carried out a number of test calculations for quarter five-spot flows that demonstrate second-order temporal accuracy, along with spatial accuracy between fourth and sixth order, depending on the relative importance of convective and diffusive terms. In order to validate the complex coupling between concentration, viscosity, and velocity fields, we employ the linear stability results by Tan & Homsy (1987) for radially symmetric miscible displacements in homogeneous porous media. The radially symmetric flow closely approximates the neighbourhood of the injection well in the quarter five-spot configuration, so that we expect the linear theory to accurately predict the early phase of finger growth in the quarter five-spot geometry. For $R = 5$, i.e. an unfavourable mobility ratio of 148.4, Tan & Homsy provide both the algebraic growth rate σ and the wavenumber n_{max} (number of fingers around the azimuth) of maximum growth as a function of Pe. Specifically, when applying the linear theory for the asymptotic limit $Pe \to \infty$ to $Pe = 400$, the authors obtain $\sigma \approx 27$ and $n_{max} \approx 60$. In comparison, our simulation of a quarter five-spot flow for $R = 5$ and $Pe = 400$ (512×512 grid, $\Delta t = 10^{-5}$) after an initial transient shows a distinct region of algebraic growth, as can be seen from the data for the vorticity maximum ω_{max} presented in figure 2. The slope corresponding to the growth rate predicted by linear stability theory is indicated as well, and visual inspection shows excellent agreement. By counting the number of fingers emerging in the quarter five-spot flow, we obtain $n_{max} \approx 48$–56, which again indicates very good agreement. This test indicates that the computational method duplicates the coupling of concentration and velocity fields with high accuracy.

A major concern in the numerical simulation of unstable porous media displacements is the issue of grid orientation effects. For a careful recent analysis of this topic and a review of the pertinent literature, see Brand *et al.* (1991). The authors

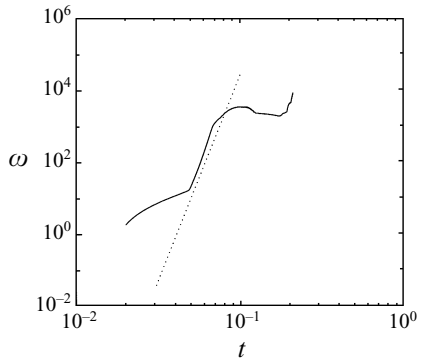

FIGURE 2. Maximum vorticity value ω_{max} in the flow field as a function of time for $R = 5$ and $Pe = 400$. Excellent agreement is observed between the growth rate of the simulation and the algebraic growth rate predicted by Tan & Homsy (1987), shown as a dotted line.

identify as the underlying cause for grid orientation effects the anisotropic nature of numerical diffusion introduced by discrete finite difference operators. As a result, grid orientation effects are shown to persist as long as the numerical diffusion is comparable to or larger than the physical diffusion, which is the case for most of the reservoir simulations reported in the literature. Our above comparison with linear stability results, on the other hand, demonstrates that, due to the high accuracy of the numerical technique, the amount of artificial diffusion introduced by the discretization is much smaller than the physical diffusion. If substantial numerical diffusion were present, an effectively lower value of Pe would result, which should affect both the algebraic growth rate and the number of emerging fingers. The excellent agreement between simulation results and linear theory thus implies that grid orientation effects are not a concern for the present simulations. The comparison with linear stability theory represents a very useful tool for obtaining information about the presence of numerical diffusion, and it should serve as a universal test case for direct numerical simulations of miscible quarter five-spot displacements.

4. Results

4.1. *Influence of Pe*

For a given combination of fluids, the value of Pe is directly proportional to the flow rate. Small flow rates provide diffusion with enough time to smear out the concentration field, whereas for larger flow rates steeper concentration gradients can be maintained. While the findings by Tan & Homsy (1987) as well as Yortsos (1987) regarding algebraic growth for radial source flow are expected to be relevant to the present investigation, the quarter five-spot flow differs from the radial source flow in two important aspects. First of all, even near the injection well the flow geometry is not perfectly radial, so that the axially symmetric base state investigated by Tan & Homsy will never be fully established. As a result, strictly speaking there is no 'base flow' solution to the governing equations, which could be analysed for the development of instabilities. However, since the quarter five-spot flow asymptotically approaches a radial source flow near the injection well, we expect to observe strong similarities to the radial source flow in this region. This is confirmed by the above comparison with linear stability theory. Hence we will refer to the 'base flow' and its 'instabilities' even for the quarter five-spot case, while keeping the above limitations in

mind. In addition, the flow domain is of finite extent, so that any emerging unstable flow features only have a finite time to grow to significant amplitudes. These points should be kept in mind for the following discussion of a series of simulations with increasing values of Pe. Throughout all of these calculations, the mobility ratio is held constant at $R = 2.5$. As initial condition for the concentration field, the self-similar distribution of the radially symmetric flow (Tan & Homsy 1987) is specified for time $t_i = 0.02$. As a result, the front is initially located at a distance of 0.2 from the injection well. The influence of the initial time t_i on the results will be discussed in detail below.

We begin by describing the flow for $Pe = 200$, which was simulated using a 384×384 grid and a time step of 10^{-4}. Figure 3(*a*) shows the concentration field for times 0.1 and 0.3072. During the early stages of the flow, we observe a nearly axisymmetric migration of the front, which at the same time spreads diffusively. Compared to rectilinear flow, however, the effects of diffusion are partially compensated by the strain field, which tends to steepen the front. Around $t = 0.2$, the deviation of the quarter five-spot flow from a purely radial source flow becomes clearly visible. Near the centre of the flow field, the concentration front encounters relatively large flow velocities in the diagonal direction, which accelerate the front towards the production well. In contrast, the front enters regions of smaller flow velocities along the edges of the domain, as it approaches the stagnation points located in the upper left and lower right corners. The differences in the propagation velocities of neighbouring front segments lead to an overall stretching of the front, which is particularly pronounced near the main diagonal. As a result, the frontal regions located there become quite steep as they approach the production well. Breakthrough, which we define as the time when the $c = 0.1$ contour reaches the production well, occurs around $t_b = 0.307$. The breakthrough recovery η is defined as

$$\eta = \frac{t_b \pi}{2}; \tag{4.1}$$

η represents the ratio of the breakthrough time t_b and the dimensionless time $2/\pi$ needed by the source to produce enough fluid to fill the entire computational domain. Phrased differently, the breakthrough recovery indicates the fraction of resident fluid displaced from the reservoir by the time of breakthrough.

A better understanding of the underlying flow dynamics can be obtained by analysing the vorticity and streamfunction fields. Figure 3(*b*) shows vorticity contours for times 0.1 and 0.3. We observe the growth of a symmetric dipole distribution, which takes the form of a concentrated pair of vortex sheets at later times. The rapid strengthening of these sheets is due to the increasing misalignment between the velocity and the concentration gradient vectors, cf. equation (2.14). The perturbation streamfunction associated with this vorticity distribution (shown in figure 3*c* for $t = 0.3$) has the form of a 'double eddy', which augments the potential base flow along the diagonal, while retarding the front propagation along the edges. The streamfunction of the potential base flow is depicted in figure 3(*d*), while figure 3(*e*) shows the superposition of base flow and perturbation. The bunching of the streamlines along the diagonal near the production well indicates the locally large velocities, which lead to the accelerated breakthrough compared with the potential flow. Notice that both the vorticity distribution and the perturbation streamfunction exist solely as a result of the viscosity contrast between the two fluids. From the investigations of Rogerson & Meiburg (1993*a*,*b*) we can conclude that the drawn out segments of the front near the production well are quite stable, since they are subject to small normal velocities and strong shear.

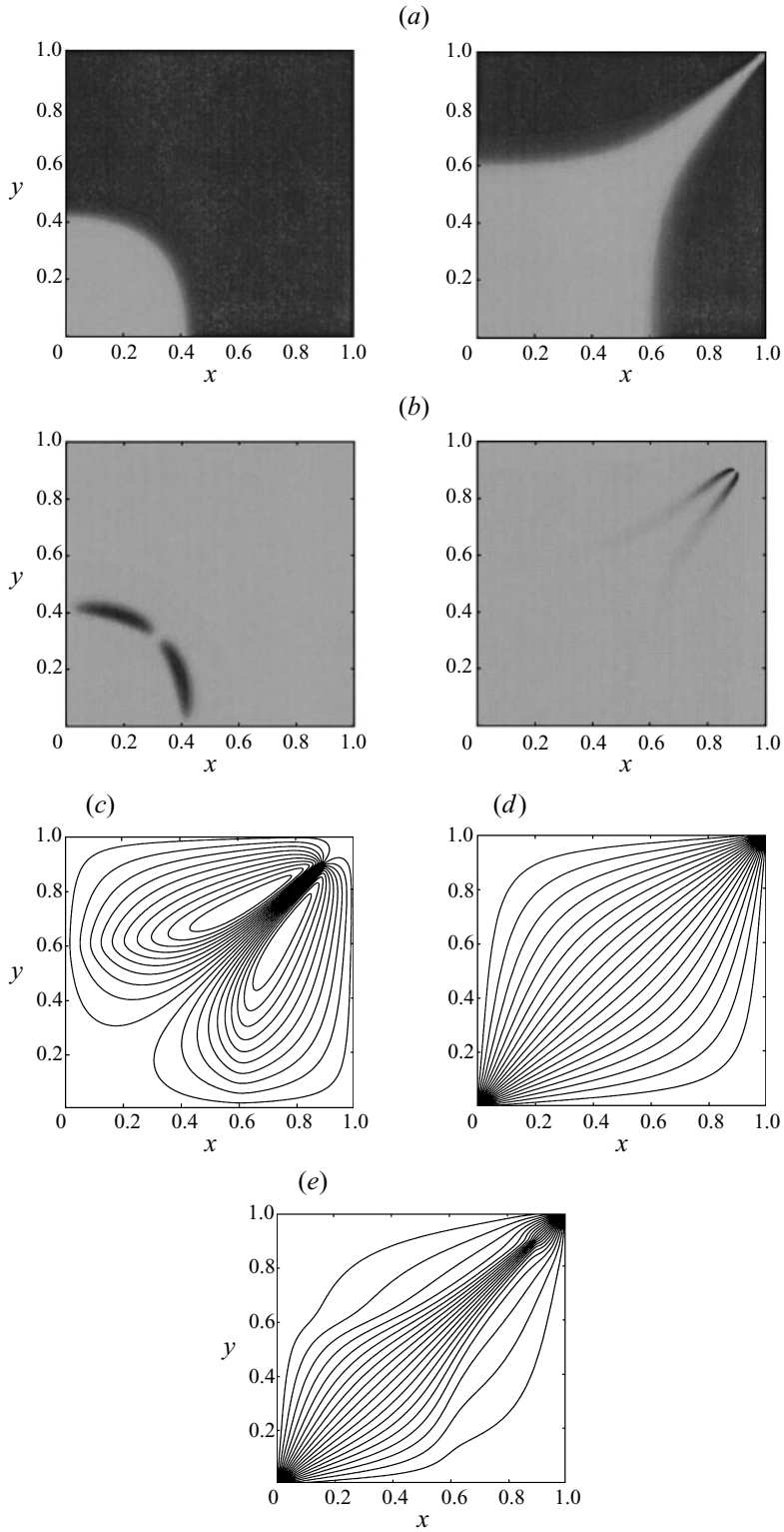

FIGURE 3. For caption see facing page.

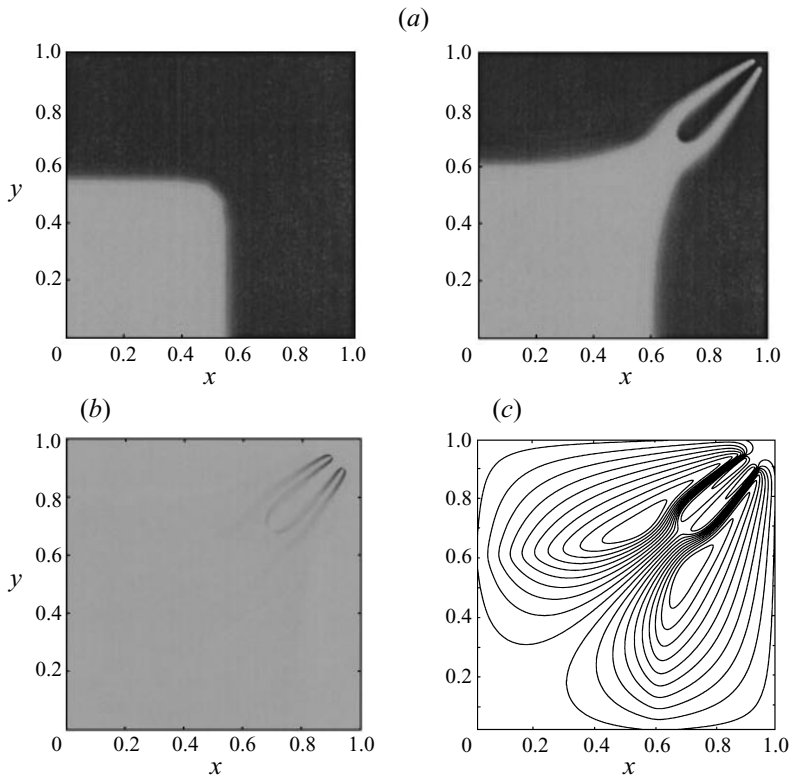

FIGURE 4. $R = 2.5$ and $Pe = 400$. (*a*) Concentration contours at times 0.2 and 0.3028. A first tip splitting event occurs at this increased flow rate. (*b*) Vorticity contours at time 0.3. The tip splitting leads to the evolution of two vortex sheet pairs. (*c*) The perturbation streamfunction at $t = 0.3$ demonstrates how the tip splitting leads to a redirection of the flow away from the diagonal.

As Pe is increased to 400, several of the flow characteristics change qualitatively. The calculation now employs a 512×512 grid, along with a time step of 5×10^{-5}. Figure 4(*a*) shows the concentration contours at times 0.2 and 0.3028. As for the lower Pe case, the front propagates in a nearly axisymmetric fashion until it reaches the centre of the domain. However, in the present, larger Pe flow, this time suffices for the viscous fingering instability to grow to an amplitude that is large enough to result in a splitting of the front near the diagonal. The symmetry of the initial conditions is preserved almost perfectly, so that two equally strong fingers now propagate towards the production well, trapping some of the resident fluid in between them. The breakthrough time $t_b = 0.303$ is nearly unchanged from the earlier case.

The vorticity, shown in figure 4(*b*) for $t = 0.3$, now shows the development of an instability of the early dipole configuration, which leads to the formation of two vortex

FIGURE 3. $R = 2.5$ and $Pe = 200$. (*a*) Concentration contours at times 0.1 and 0.3072. During the early stages, the concentration front evolves in an almost radially symmetric fashion. Later, it becomes increasingly aligned with the flow direction. (*b*) Vorticity contours, scaled with the instantaneous maxima, for times 0.1 and 0.3. The initial dipole evolves into a pair of concentrated vorticity layers. (*c*) The perturbation streamfunction at $t = 0.3$ takes the form of a double eddy that enhances the potential base flow along the diagonal. (*d*) The streamfunction of the potential base flow. (*e*) Superposition of the base flow and perturbation streamfunctions.

sheet pairs, each of which propels a finger along its centre. The redirection of the flow away from the diagonal is furthermore reflected in the plots of the perturbation streamfunction (figure 4*c*) as well.

For $Pe = 800$, the dynamical complexity of the flow increases further. The concentration contours at times 0.175 and 0.267 (figure 5*a*) demonstrate the emergence of approximately sixteen fingers due to the viscous fingering instability of the nearly radial source flow. These fingers evolve solely from the perturbation provided by the small deviation of the quarter five-spot flow from the radial source flow, without any explicit triggering. The number of fingers amplified by the flow reflects the optimally growing wavenumber of the radial flow, thereby confirming the ability of the present simulations to duplicate the physical wavenumber selection mechanism known from linear stability theory. For the present large Pe, the instability grows sufficiently fast to dominate the flow before the front reaches the centre of the domain and loses its near axisymmetry. The many localized dipoles in the vorticity field, depicted in figure 5(*b*) for the same times as the concentration field, reflect the emergence of multiple fingers as well. As the unstable front reaches the central domain, the fingers undergo a nonlinear selection process. Those near the diagonal continue to exhibit vigorous growth, fuelled by the strong normal flow velocities in this region. Those fingers closer to the edges, on the other hand, reach a maximum amplitude, upon which they decay diffusively due to the decrease in the local normal velocity. In addition, some of the fingers undergo a merging event, similar to those observed in rectilinear displacements (Tan & Homsy 1988; Zimmerman & Homsy 1992; Rogerson & Meiburg 1993*b*). Both the perturbation streamfunction (shown in figure 5*c* for $t = 0.15$ and 0.267) and the overall streamfunction (depicted in figure 5*d* for the identical times) demonstrate the generation of smaller scales and more complex overall flow patterns. The breakthrough time t_b now is approximately 0.267, which is more than 10% lower than the values observed for lower Pe. This reflects the strong influence of Pe on the dynamics of the flow, and on the overall recovery rate.

For $Pe = 1200$, the generation of smaller scales in the flow field becomes even more pronounced, see figure 6. The low level of diffusion allows many fingers to grow to relatively large amplitudes, at which point some of them are affected by such nonlinear mechanisms as tip splitting and merging. As the highly distorted concentration front reaches the central regions of the flow, the four fingers nearest to the diagonal begin to outgrow their neighbours and to accelerate towards breakthrough. It is interesting to note that all four of these fingers stay in competition until very late times. In the absence of further secondary instability events such as tip splitting or side branching, they maintain long and slender shapes that resemble those observed in the experiments of Zhang *et al.* (1997).

The largest value of Pe simulated in this investigation is 2000. Concentration contours, computed on a 1024×1024 grid, are shown in figure 7(*a*) for $R = 2.5$ and a starting time of the simulation $t_i = 0.005$. In order to break the artificial symmetry about the diagonal, slightly asymmetric initial conditions are prescribed. During the early, nominally nearly axisymmetric stages, the unstable flow gives rise to numerous

FIGURE 5. $R = 2.5$ and $Pe = 800$. (*a*) Concentration contours at times 0.175 and 0.267. At this larger Pe value, a vigorous fingering instability is observed. (*b*) The vorticity field at the same times as in (*a*). (*c*) The perturbation streamfunction at times 0.15 and 0.267. (*d*) Overall streamfunction at the same times as in (*c*).

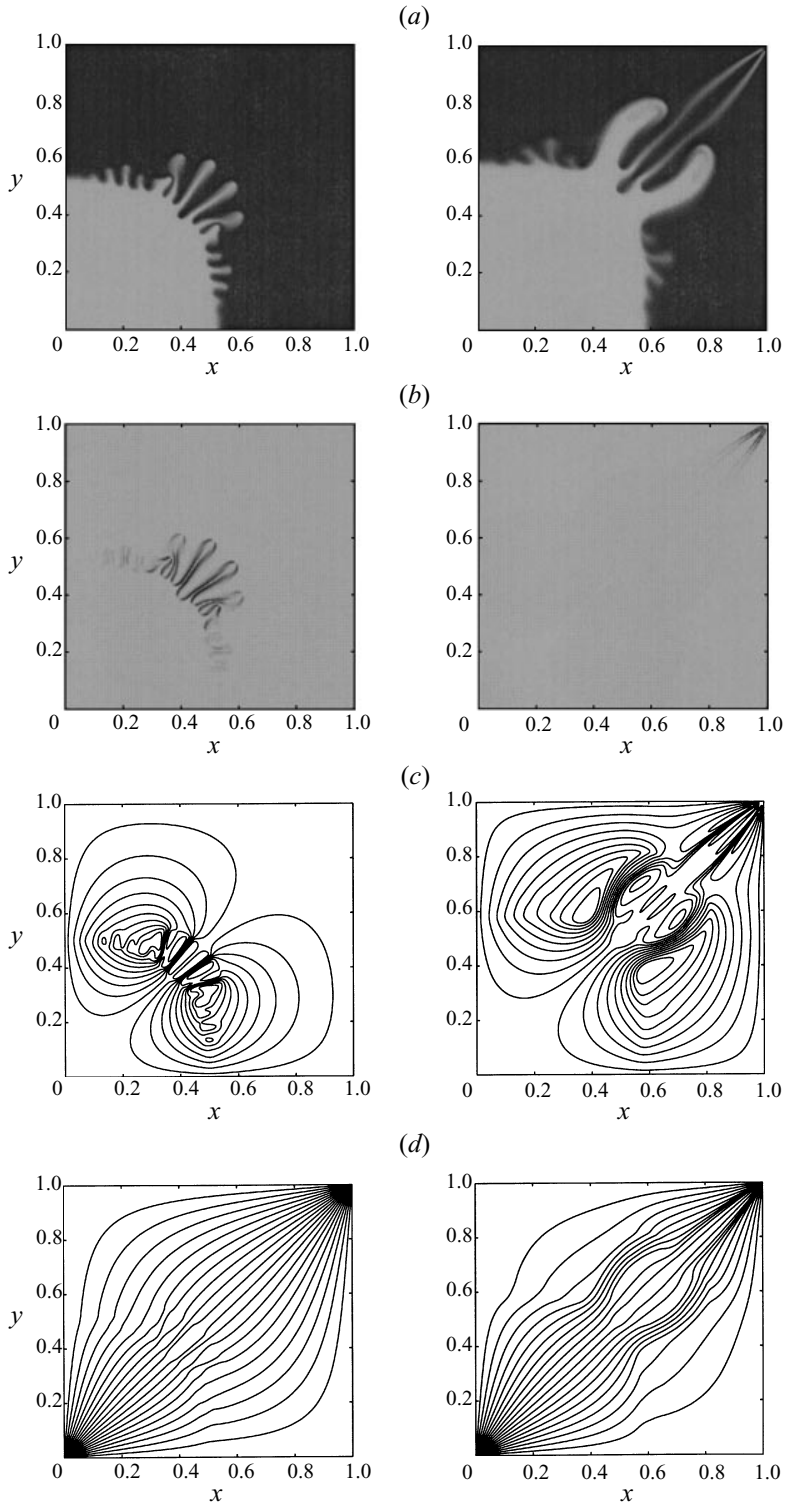

FIGURE 5. For caption see facing page.

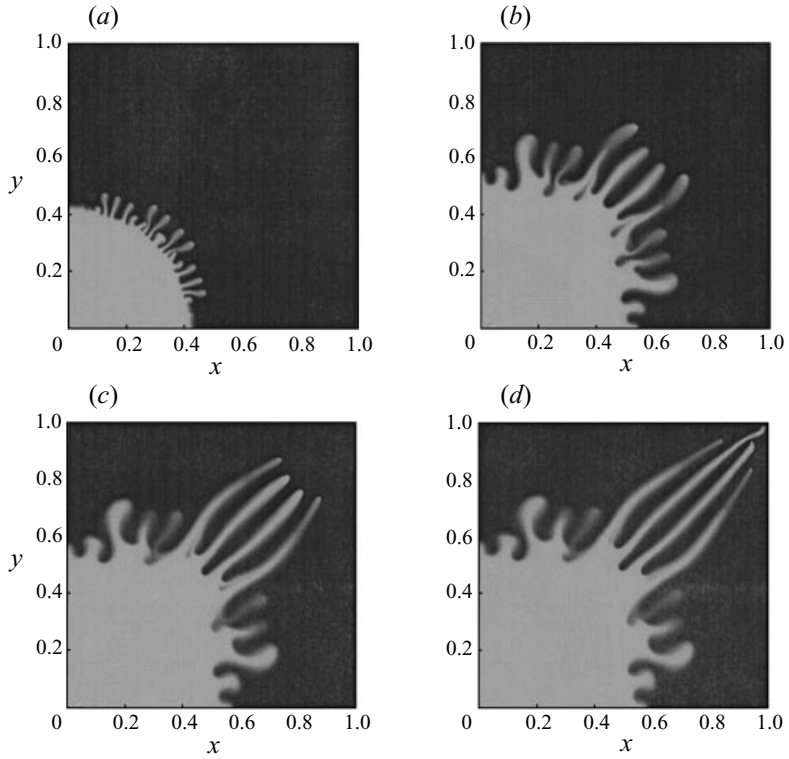

FIGURE 6. $R = 2.5$ and $Pe = 1200$. Concentration contours for times (*a*) 0.1, (*b*) 0.2, (*c*) 0.25, and (*d*) 0.2687. Several long, slender fingers stay in competition and dominate the flow until breakthrough occurs.

small fingers, which soon reach amplitudes large enough for nonlinear effects to become important. The competition between them reduces their number to $O(10)$, mostly due to shielding and merging events, and in spite of an occasional tip splitting. The remaining fingers continue to interact strongly with each other, in particular through partial merging, shielding, and splitting events. In the process, several small islands of resident fluid are formed and left behind. In contrast to the lower Pe simulations, the fingers near the edges of the domain keep growing until later times, in spite of the eventual dominance by those fingers located near the diagonal.

It is of interest to note the fairly short time scale of the nonlinear selection mechanism that decides which finger will eventually break through first. As late as $t = 0.160$, there are still several fingers that appear to have a chance to win the overall competition. However, by $t = 0.200$, a clearly dominant finger has emerged, and by $t = 0.240$ breakthrough occurs. During the final stages, the dominant finger accelerates considerably, which triggers several additional tip-splitting events that lead

FIGURE 7. $R = 2.5$ and $Pe = 2000$. (*a*) Concentration contours at times 0.05, 0.1, 0.200 and 0.240. After the formation of many fingers during the initial stages, nonlinear interactions lead to a reduction in their number. Shortly before breakthrough, the acceleration of the dominant finger leads to a renewed generation of small scales. (*b*) The perturbation streamfunction at $t = 0.240$. (*c*) The overall streamfunction at $t = 0.240$. (*d*) Velocity magnitude contours at $t = 0.240$.

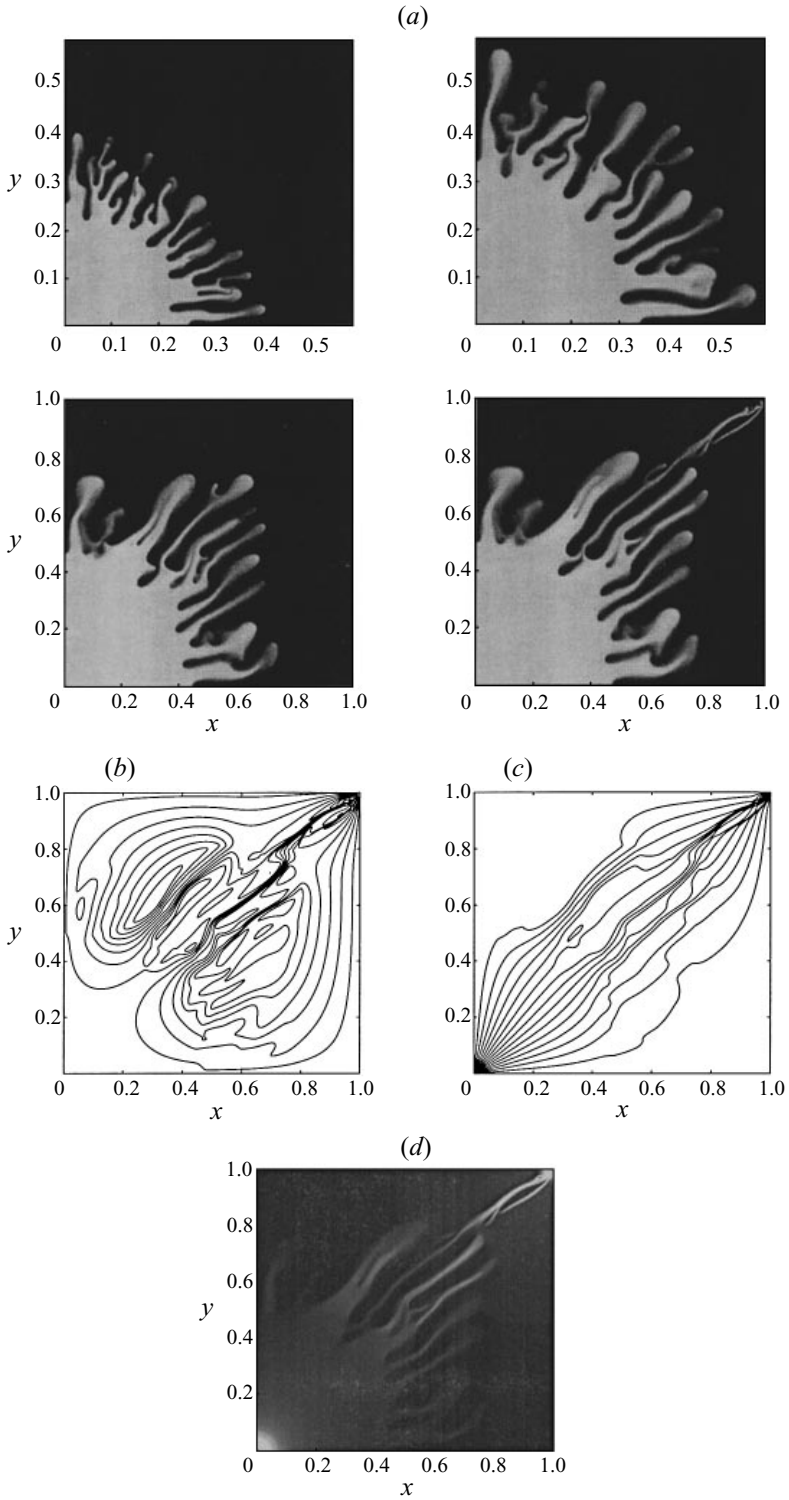

FIGURE 7. For caption see facing page.

to the generation of fairly small scales near the production well. Most of the flow field remains frozen during the last stages and shows very little change after $t \approx 0.16$.

The dominant scales of the flow field show an interesting dependence on space and time. During the early phase, the linear instability of the nearly radially symmetric flow gives rise to many fingers of very small size near the injection well. Subsequently, merging, shielding, and diffusion, in combination with the slowdown of the front in the central region, eliminates many of the small-scale features, so that the dominant length scale grows dramatically. Eventually, however, as the dominant finger accelerates towards the production well, its instability produces smaller scales in this region again.

Figures 7(*b*) and 7(*c*) show the perturbation streamfunction and the overall streamfunction, respectively. While globally the perturbation streamfunction still has the character of a dipole, it now exhibits many additional smaller-scale structures, which reflect the channelling of the injected fluid through the evolving fingers. The overall streamfunction also indicates preferred paths for the flow, as does the contour plot for the velocity magnitude shown in figure 7(*d*). This graph indicates that at the breakthrough time only a few, long and narrow regions have a sizeable fluid velocity, whereas everywhere else the fluid is essentially at rest. It is interesting to note that there is not a single, connected channel for the fluid, but rather a few almost disconnected segments. Consequently, the velocity field has to keep evolving even beyond the breakthrough time, although this was not explored in the present investigation.

The above simulations show that for Pe-values sufficiently large to support viscous fingering, the flow evolves through distinct stages. Early on, while the growing perturbations are still small, the intial concentration front spreads in a nearly radially symmetric fashion, its thickness being determined by the competition of molecular diffusion and strain. After a time that decreases with increasing Pe, the emergence of many viscous fingers becomes the dominant feature. These fingers undergo algebraic growth in quantitative agreement with the linear stability results for radial source flow. Once the fingering instability has reached a certain amplitude, nonlinear effects gain importance, which lead to the selection and preferential growth of one or a few fingers near the diagonal. These fingers subsequently undergo a strong acceleration, until they break through at the production well.

The different dynamical evolutions are reflected in the time-dependent growth of the maximum vorticity value ω_{max} in the flow field, which is shown in figure 8 for $R = 2.5$ and various Pe. The interaction of the radially symmetric initial condition for the concentration field with the slightly non-radially symmetric potential velocity field causes finite-strength vorticity to be present from the very start. During the early stages, its maximum grows slowly as the 'base flow' develops. For relatively small Pe-values, the time scale associated with the growth of the instability is not small compared to the time scale of the overall quarter five-spot flow, so that a region of algebraic growth does not evolve. With increasing Pe, however, those spectral components of the initial vorticity that correspond to the eigenfunctions of the radially symmetric linear stability problem, are strongly amplified in an algebraic fashion and soon begin to dominate the evolution. Hence, for those simulations that develop a viscous fingering instability, the vorticity maximum undergoes a period of algebraic growth, whose growth rates are in excellent agreement with the predictions by Tan & Homsy's (1987) linear stability investigation for radial source flow. With increasing values of Pe, the amplification rates increase, and the evolution of the flow becomes dominated by algebraic growth at earlier times. At maximum vorticity values that increase with Pe, all calculations show some nonlinear saturation.

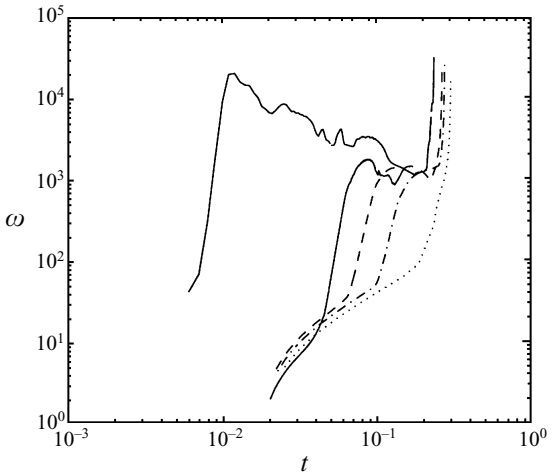

FIGURE 8. $R = 2.5$. Maximum vorticity value ω_{max} in the flow field as a function of time for various Pe-values. From right to left, the curves are for $Pe = 400$, 600, 800, 1200, and 2000. All calculations started at the identical time of 0.02, except for the case $Pe = 2000$, which started at $t = 0.005$. Small Pe do not result in an algebraic growth regime. Larger Pe-values give rise to a fingering instability, whose algebraic growth sets in earlier with increasing Pe.

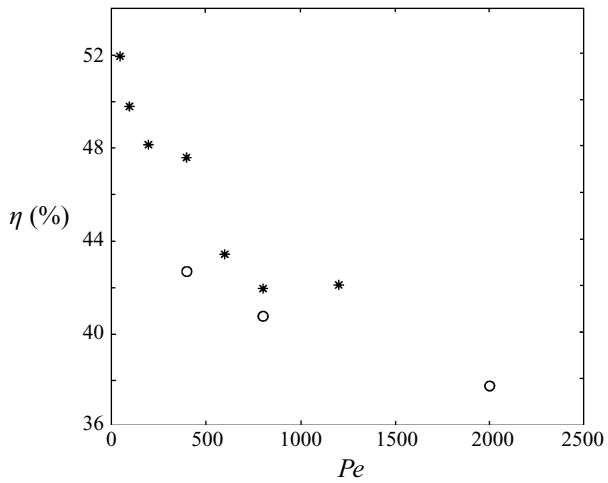

FIGURE 9. $R = 2.5$. Recovery at breakthrough in per cent, as a function of Pe. $*$, $t_i = 0.02$; $\circ$, $t_i = 0.005$.

Figure 9 depicts the recovery at breakthrough as a function of Pe, for $R = 2.5$ and $t_i = 0.02$, where breakthrough is defined as the time at which the $c = 0.1$ contour reaches the production well. The qualitatively different flow regimes described above strongly affect this efficiency. For relatively small Pe-values, the efficiency decreases with increasing Pe, before levelling off somewhat around $Pe \approx 400$. As Pe increases further, more and more vigorous fingering ensues, which leads to a renewed drop in efficiency, followed by another levelling off above $Pe \approx 800$. The $Pe = 2000$ simulation shows a further drop in efficiency. However, this simulation started at an earlier time, and it employed slightly asymmetric initial conditions, so that the comparison with the lower Pe calculations is of limited value here. Regarding the effects of simulation

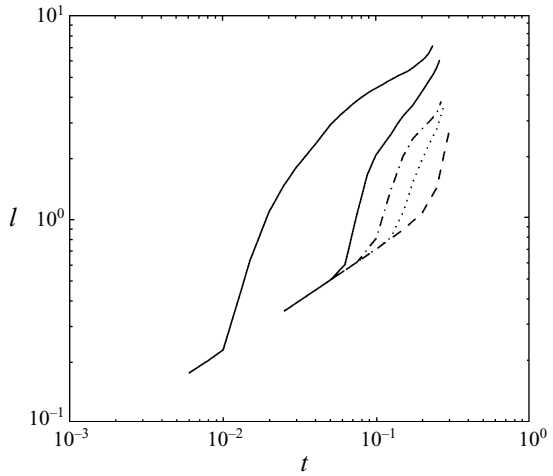

FIGURE 10. $R = 2.5$. The interfacial length, measured as explained in the text, as a function of time for various Pe-values. From right to left, the curves are for $Pe = 400$, 600, 800, 1200, and 2000. All calculations started at time 0.02, except $Pe = 2000$, which started at $t_i = 0.005$. The more rapid growth of the interfacial lengths observed for higher Pe-values reflects the distortion of the interface due to viscous fingering.

starting time and asymmetry, more information will be provided below. In any case, our data provide some support for the observation by Brock (1990) that for very large Pe values the global flow features become increasingly independent of Pe, even though the dynamics of the flow continues to change at the small-scale level.

An interesting quantity is the length of the interface separating the two phases. Strictly speaking, of course, such an interface is not defined for the present case of miscible flow. However, the quantity

$$L(t) = \int_0^1 \int_0^1 (c_x^2 + c_y^2)^{1/2} \mathrm{d}x \, \mathrm{d}y \tag{4.2}$$

provides a good measure of the overall length $L(t)$ of the diffusive region between the two fluids. Its growth is shown in figure 10 for $R = 2.5$ and several different Pe-values. During the initial stages, when the interface is of nearly circular form, its length grows according to

$$L(t) \sim t^{1/2} \tag{4.3}$$

in all simulations. Later, however, the asymmetry of the base flow as well as the vorticity in the flow field lead to a distortion of this circular shape, and thereby to a faster interfacial growth. As a general tendency, the interface becomes more convoluted as Pe increases, which is reflected by the larger values of its length.

4.2. *Influence of mobility ratio*

The second dominant dimensionless parameter governing the overall evolution of homogeneous flows is the mobility ratio R. Its influence can best be analysed by discussing a series of simulations employing different values of R, for which Pe is held constant.

The case $R = 0$, $Pe = 400$ displayed in figure 11 shows the passive convection of the concentration field in the potential quarter five-spot flow. Since both fluids have identical viscosities, no vorticity is being generated (de Josselin de Jong 1960), so

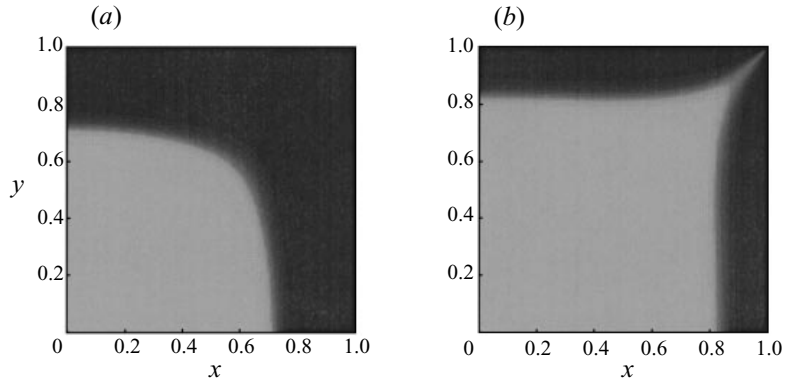

FIGURE 11. Concentration field for $R = 0$ and $Pe = 400$. Shown are the contours for times (*a*) $t = 0.3$, and (*b*) 0.4570. In the absence of a viscosity contrast, the concentration field is passively convected along by the irrotational velocity field.

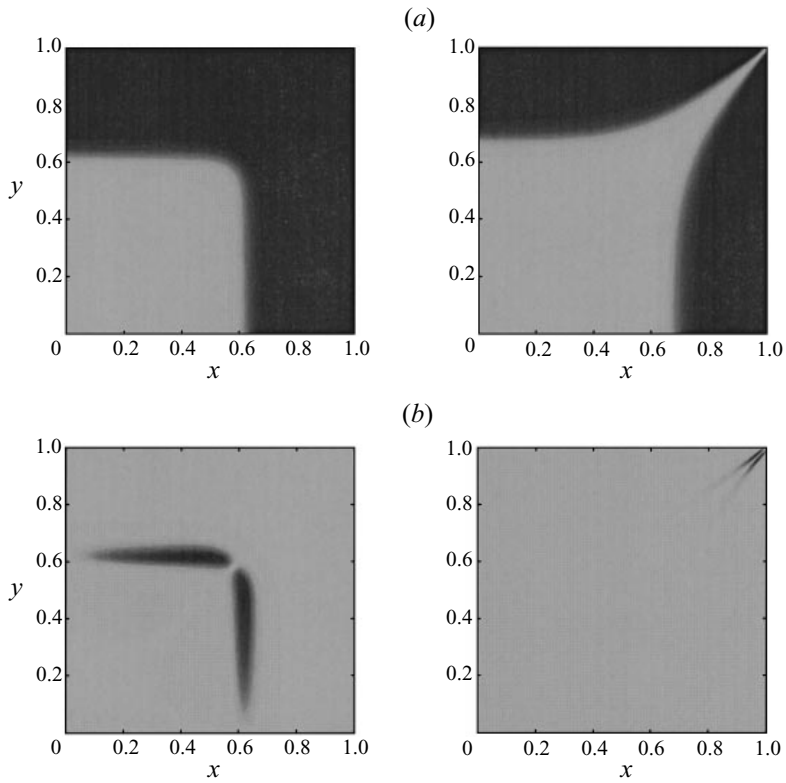

FIGURE 12. $R = 1.5$ and $Pe = 400$. (*a*) Concentration contours at times 0.25, and 0.3484. (*b*) Vorticity field at the same times.

that the velocity field remains potential and does not change with time. Breakthrough occurs around $t_b = 0.4570$, in agreement with the prediction by Morel-Seytoux (1965).

Any non-vanishing value for R renders the flow field rotational, see figure 12(*a*), which for $R = 1.5$ shows the concentration contours at times 0.25 and 0.3484, when breakthrough occurs. The main difference compared to the $R = 0$ case lies in the

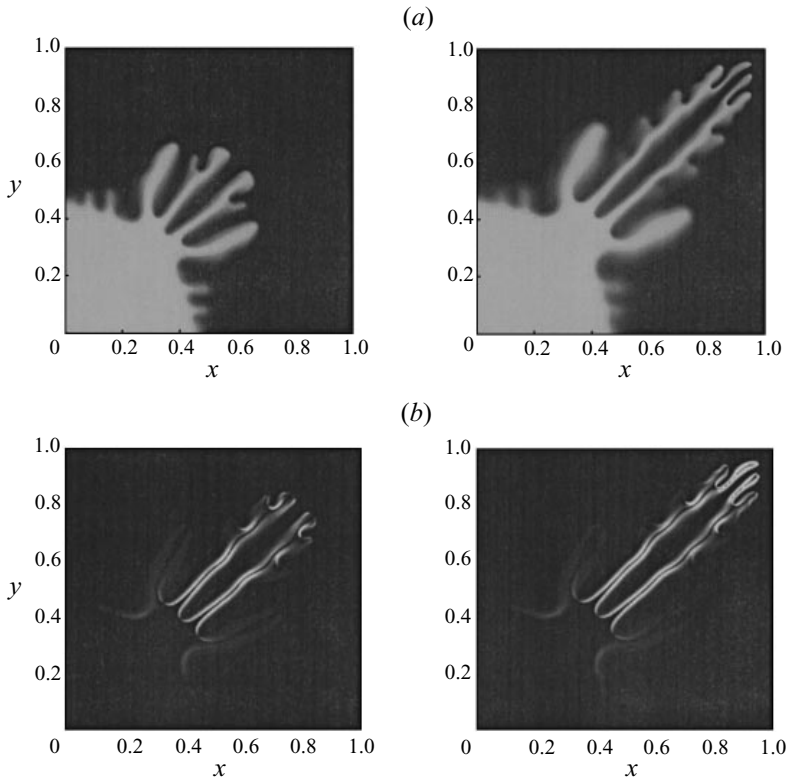

FIGURE 13. $R = 5$ and $Pe = 400$. (*a*) Concentration contours at times $t = 0.16$, and 0.2145. (*b*) Vorticity field at times $t = 0.20$ and 0.2145. At this large mobility ratio, the fingers undergo secondary tip-splitting and side-branching instabilities.

slowdown of the concentration front near the edges of the domain, and the speedup of the central finger towards the production well. These features, which result in an earlier breakthrough, and thus in reduced recovery, can again be understood best in terms of the vorticity (figure 12*b*) field. It indicates that the interaction of the velocity and viscosity fields leads to the formation of an elongated vorticity dipole, which in turn creates a 'double eddy' that modifies the base flow. This eddy increases the velocity along the diagonal, while slowing down the flow near the domain edges, thereby leading to the observed respective acceleration and deceleration of different parts of the front. The intense stretching of the front as it approaches the production well leads to steep concentration gradients in this region.

As R is increased further and Pe is held constant, the tendency of the flow to develop instabilities increases, as can be seen from the simulation for $R = 2.5$ and $Pe = 400$ described in figure 4. By further raising the value of R to 5, we trigger an even more vigorous growth of the viscous fingering instability. As the concentration contours of figure 13(*a*) ($t = 0.16$ and 0.2145) show, a number of fingers develop initially, of which those closest to the main diagonal reach large amplitudes. The two central fingers subsequently undergo repeated tip splitting events, a secondary instability that has also been observed in rectilinear flows (Tan & Homsy 1988; Zimmerman & Homsy 1992; Rogerson & Meiburg 1993*b*). In the process, they furthermore begin to shield their off-diagonal neighbours, thereby preventing them from growing further, again in close similarity to rectilinear flows (Tan & Homsy 1988).

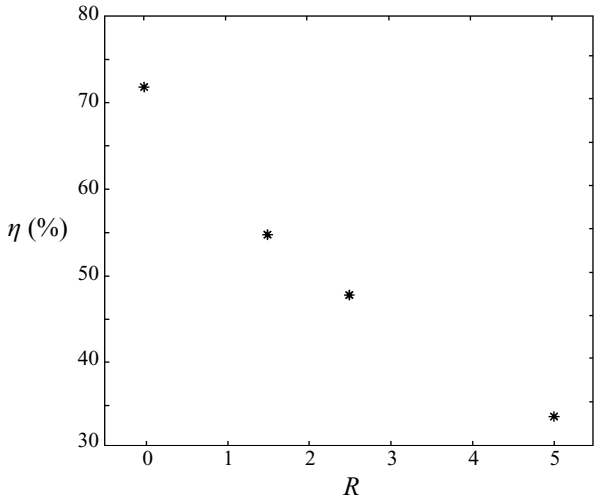

FIGURE 14. Recovery at breakthrough as function of the mobility ratio R, for $Pe = 400$ and $t_i = 0.02$. The recovery decreases uniformly with increasing values of R.

The tendency of fingers to undergo tip splitting events is a function of the local velocity field near the finger tip, and thus partially of the underlying potential flow field. When compared to the rectilinear flow investigated by Tan & Homsy (1988), the potential flow is quite different for the quarter five-spot flow, where it varies spatially. Specifically, near the injection well the strain field of the irrotational flow tends to widen the finger tip, which should promote splitting. However, since for the present simulation parameters the fingers have not grown to large enough amplitudes yet, the simulation does not show any tip splitting near the injection well. Near the production well the potential flow has the effect of narrowing the finger tips, which tends to stabilize them. Due to the large velocities in this region, however, the simulation still shows repeated splitting, even as the fingers approach the production well. In the centre of the domain, where we observe the first tip splitting, the potential flow resembles uniform rectilinear flow.

The tip splitting events are reflected in the vorticity contours as well, which are shown in figure 13(*b*) for times 0.20 and 0.2145. These plots furthermore demonstrate how the shielded fingers become increasingly passive. Most of the vorticity, which can be regarded as a 'source' of velocity, is concentrated in the active regions near the finger tips.

Figure 14 indicates that the recovery at breakthrough decreases significantly as a function of the mobility ratio R for $Pe = 400$ and t_i=0.02. However, one has to keep in mind that the three data points correspond to very different flow regimes. For $R = 1.5$, no fingering occurs, for $R = 2.5$ one splitting is observed, and for $R = 5$ the flow evolves under a vigorous fingering instability. A comparison of the recoveries for different R at values of Pe that result in similar flow regimes would show a much weaker dependence of the recovery on the mobility ratio.

4.3. *Influence of the initial conditions*

As shown above, the overall dynamical evolution of the flow field changes dramatically if the fingering instability grows to amplitudes that are large enough to dominate the flow. The radially symmetric initial concentration field by itself does not contain

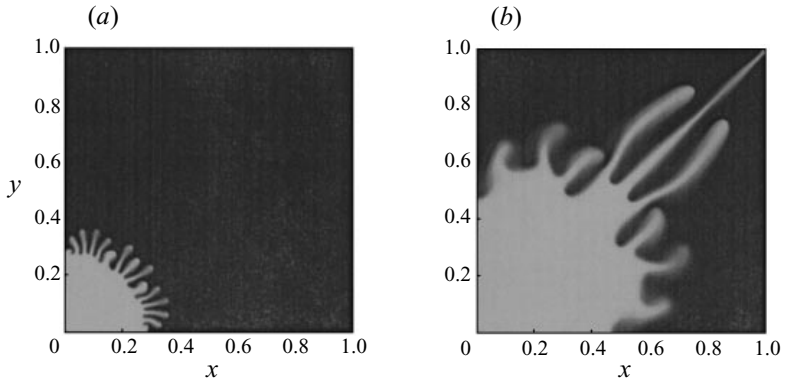

FIGURE 15. $R = 2.5$, $Pe = 800$, and $t_i = 0.005$. Concentration contours at times (*a*) 0.05, and (*b*) 0.2599. Except for the smaller starting time of the simulation, all parameters are identical to the calculation shown in figure 5. The earlier starting time leads to an earlier and more vigorous development of the fingering instability.

any perturbations that could trigger this instability. However, as discussed above, the potential velocity field near the injection well differs slightly from a purely radial source flow. At the start of the simulation, this small difference is sufficient to trigger the fingering instabilities by inducing a perturbation in the concentration field as well. This concentration perturbation grows from very small initial amplitudes with an algebraic growth rate that depends on R and Pe only. Obviously, the instability can start its growth only from the time for which the initial conditions have been specified. It hence seems reasonable to ask if the instability can grow to larger amplitudes in a simulation that starts at an earlier time, since this would provide the instability with more time to grow. This is indeed the case, as the concentration contours in figure 15 ($R = 2.5$, $Pe = 800$, times 0.05 and 0.2599) show. Here the starting time of the simulation is $t_i = 0.005$, instead of $t_i = 0.02$ for the simulation depicted in figure 5. All other parameters are identical. For the earlier starting time, vigorous fingering sets in much earlier and has reached much larger levels by $t = 0.1$. The subsequent phase of deceleration near the edges, as well as acceleration and breakthrough along the diagonal, however, proceeds quite similarly for both flows, and the breakthrough time for the simulation started earlier is only about 3% smaller. This result indicates that for the present set of parameters the earlier starting time has only a small effect on the overall recovery rate, in spite of triggering much more intense early fingering.

The situation is somewhat different for $R = 2.5$ and $Pe = 400$. The concentration contours for $t_i = 0.005$ (shown in figure 16 for times 0.095 and 0.2717) should be compared with those given in figure 4 for $t_i = 0.02$. We now observe a qualitative change as a result of the earlier starting time. While for $t_i = 0.02$ only a single bifurcation of the front occurs, a starting time of $t_i = 0.005$ results in the development of eight fingers at an early stage. Their interaction leads to a breakthrough time of about 0.2717, which is approximately 10% less than for the later starting time. Note in particular that the difference between the breakthrough times is several times larger than the difference between the simulation starting times. The difference in these simulations is due exclusively to the longer time interval available for the perturbations to grow. For the earlier starting time, this interval is sufficiently long for the perturbations to grow into eight large-amplitude fingers.

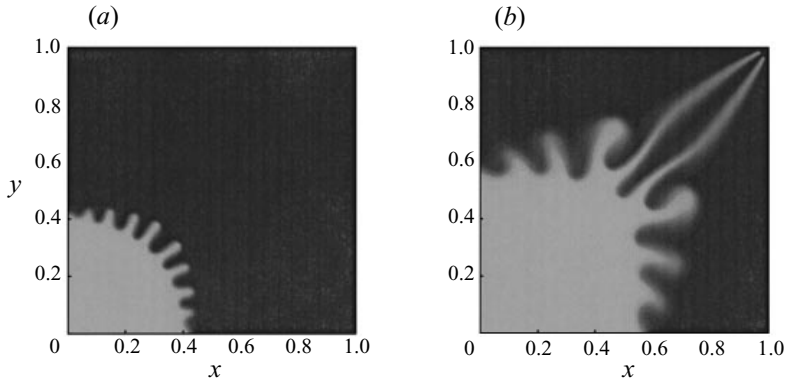

FIGURE 16. $R = 2.5$, $Pe = 400$, and $t_i = 0.005$. Concentration contours at times (*a*) 0.095, and (*b*) 0.2717. Except for the smaller starting time of the simulation, all parameters are identical to the calculation shown in figure 4. The earlier start leads to the growth of eight fingers (as opposed to a single splitting for the later starting time). As a result, the time until breakthrough is reduced by approximately 10%.

All of the above simulations except for the one at $Pe = 2000$ employed initial conditions that are symmetric with respect to the main diagonal. Any non-symmetric truncation and roundoff errors were typically not able to break this symmetry until very late in the simulation, so that it persisted until close to breakthrough. It is of interest, however, to explore whether or not non-symmetric initial conditions might lead to a significantly different behaviour. The simulation shown in figure 17 addresses this issue. For $R = 2.5$ and $Pe = 400$, it employs a nearly radially symmetric initial concentration front, whose radius varies smoothly between $r_i = 0.1$ in the y-direction and $r_i = 0.102$ in the x-direction. This simulation should be compared with the one in figure 16, where $r_i = 0.1$ everywhere. Figure 17 shows the instability to grow faster along the x-axis than along the y-axis. Again, a competing pair of dominant fingers evolves near the diagonal, with the one above the diagonal breaking through first. The breakthrough by an above diagonal finger in spite of the stronger early instability growth below the diagonal is a reflection of the complex nonlinear evolution of the flow. It is interesting to note that the breakthrough time, and hence the recovery, in this particular case changes by less than 1% as a result of the asymmetry, although one has to keep in mind that this asymmetry is fairly small here. Figure 18 summarizes the recovery data as a function of R, Pe, t_i, and symmetric or non-symmetric initial conditions.

4.4. *Time-dependent injection rate*

The above simulations show that a vigorous fingering instability develops mostly during the early stages, when the flow is still nearly radial, and the flow velocities are directed approximately normal to the concentration front. During the later stages the most advanced sections of the front, with the exception of the tip itself, increasingly align themselves with the direction of the fluid flow, thereby becoming subject to strong shear. This in turn stabilizes the front (Rogerson & Meiburg 1993*a*), so that a fingering instability is less likely to develop during the later stages of the quarter five-spot flow. Based on this behaviour, we can design a strategy for potentially enhancing the recovery at breakthrough. Especially the simulations shown in figures 4 and 16 suggest that the breakthrough time for a particular combination of R and Pe can be delayed significantly if the growth of the fingering instability can be suppressed during the early stages. This would indicate that the breakthrough recovery of a

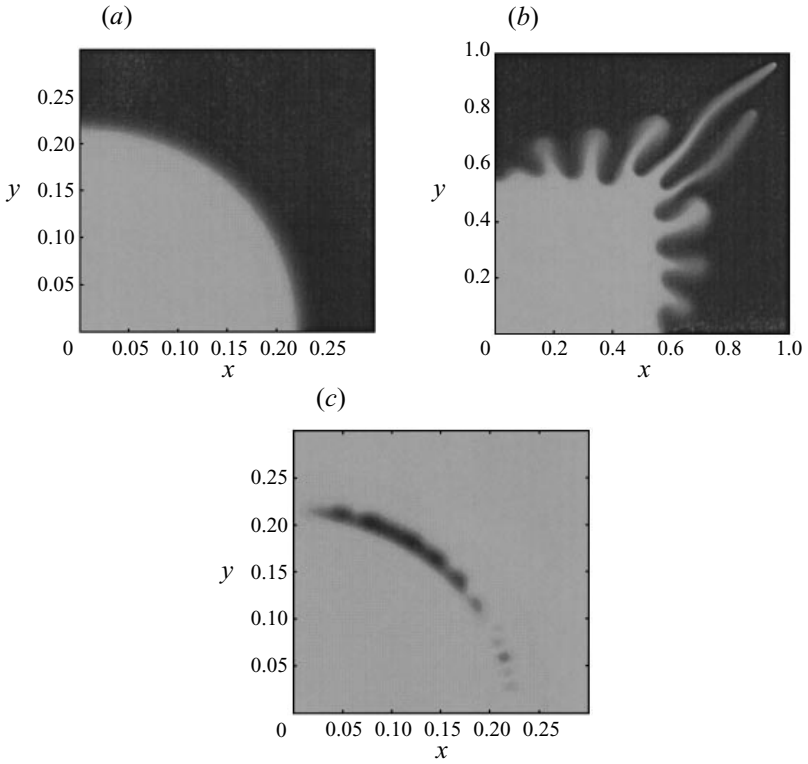

FIGURE 17. $R = 2.5$ and $Pe = 400$. In order to break the symmetry of the evolving flow field, the initial radial location of the concentration front is specified such that it varies between $r_i = 0.1$ in the y-direction and $r_i = 0.102$ in the x-direction. Concentration and vorticity contours are shown for time 0.025. While the asymmetric evolution is reflected by the concentration contours at time 0.2721, its effect on the breakthrough time is less than 1%.

constant-flow-rate process could be improved by starting with a smaller flow rate and subsequently increasing it, so that averaged over time it reaches the same level as that of the constant-flow-rate case. Formulated differently, we ask if, for a prescribed overall process time, the injection rate can be optimized as a function of time in order to maximize the breakthrough recovery.

The above ideas are explored in more detail in the calculation shown in figure 19, which shows results for a time-dependent injection rate. Since the characteristic time scale $L^2/Q(t)$ now varies with time, it is easier to argue in terms of injected pore volume q, rather than dimensionless time; q represents the total amount of fluid injected as a fraction of the total area of the domain. In order to be able to compare the present, variable-injection-rate results with the above constant-injection-rate simulations, we again employ $r_i = 0.2$ and $R = 2.5$. Pe now varies between 400 and 800 as follows. Up until $q = 0.1571$, Pe is held constant at a value of 400. Subsequently, it is continuously increased in a smooth fashion, until it reaches 800 at $q = 0.2356$. Figure 19 shows the concentrations contours for $q = 0.334$ and 0.468. The present calculation should be compared with those for $Pe = 400$ and 800 shown in figures 4 and 5. Due to the lower initial injection rate, the variable-Pe calculation does not result in the formation of many small fingers, such as those seen in the $Pe = 800$ calculation. Instead, only one splitting occurs, and breakthrough does not take place until $q_b \approx 0.468$. This value for

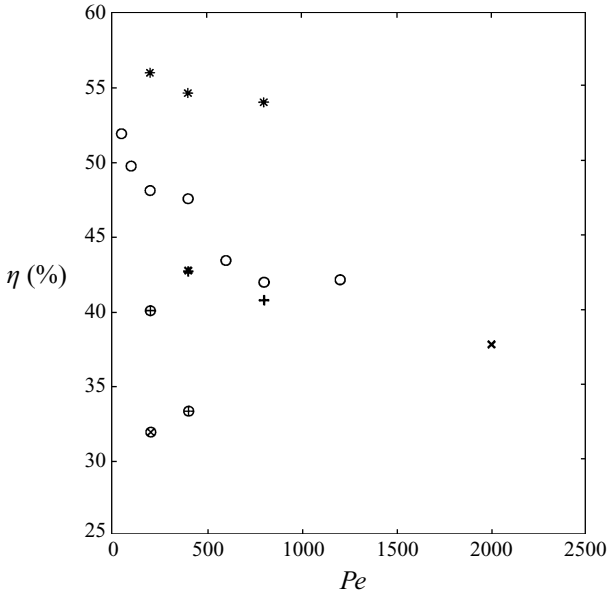

FIGURE 18. Summary of recovery data as a function of R, Pe, t_i, and symmetric or non-symmetric initial conditions. $*$, R=1.5, t_i=0.02, symmetric; $\circ$ R=2.5, t_i=0.02, symmetric; $\oplus$, R=5, t_i=0.02, symmetric; $+$, R=2.5, t_i=0.005, symmetric; $\otimes$, R=5, t_i=0.005, symmetric; $\times$, R=2.5, t_i=0.005, asymmetric.

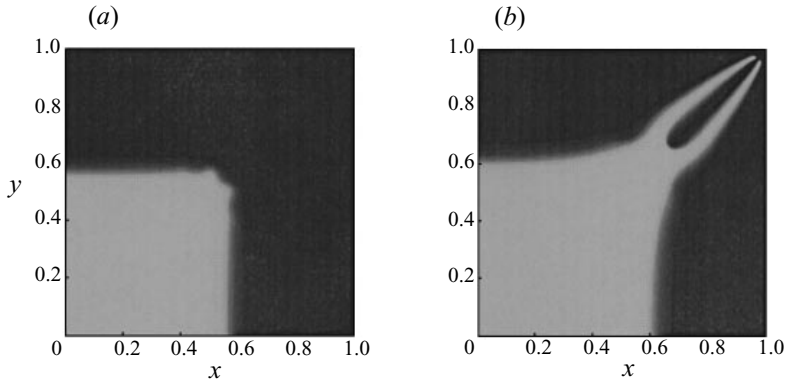

FIGURE 19. $R = 2.5$ and $t_i = 0.02$ with time-dependent injection rate. Over the course of the simulation, the initial Pe-value of 400 is increased to 800. Shown are the concentration contours at injected pore volumes q of (*a*) 0.334, and (*b*) 0.468. The low Pe-value during the early stages prevents the development of a strong fingering instability. Since larger Pe-values at later times are unable to trigger strong fingering, the breakthrough efficiency of the variable-injection-rate process is enhanced by approximately 8% compared to a constant-injection-rate process of equal overall duration.

q_b is to be compared with $q_b(Pe = 400) \approx 0.4757$, $q_b(Pe = 600) \approx 0.4342$ (not shown), and $q_b(Pe = 800) \approx 0.4194$. Consequently, replacing the $Pe = 600$ process with one of different instantaneous, but nearly identical average injection rate, leads to an increase of the recovery at breakthrough of almost 8%. In fact, the breakthrough recovery is only slightly smaller than for the $Pe = 400$ simulation, indicating that the increase in the flow rate at later times has an almost negligible effect.

The important conclusion to be drawn from the above simulation is that the breakthrough recovery is much more adversely affected by large Pe-values during the early stages of the quarter five-spot flow. Large flow rates during the later stages, on the other hand, do not decrease the efficiency by much. It is to be kept in mind, however, that the present investigation is based on molecular diffusion only, while velocity-dependent dispersion effects are not accounted for. The work by Koch & Brady (1987, 1988), on the other hand, demonstrates that in realistic porous media the effective diffusion coefficient can become proportional to the macroscopic flow velocity, thereby rendering the Pe value independent of the injection rate.

5. Discussion and conclusions

The high-accuracy direct numerical simulations described above provide information on the dynamical evolution of miscible homogeneous quarter five-spot displacements at a high level of detail. By resolving all length scales of the flow, they accurately reproduce the governing physical mechanisms, as well as the interactions among them, as a function of the mobility ratio and the dimensionless flow rate. The present investigation explores the influence of these parameters up to values of $R = 5$ and $Pe = 2000$. Due to the external length scale prescribed by the quarter five-spot configuration, perturbations only have a finite time span available during which they can evolve into large-scale fingers. As a result, for small viscosity contrasts and moderate Pe-values, i.e. for stable flows or flows characterized by weak instability, a visible fingering instability does not evolve, and breakthrough occurs at a relatively late time, so that the recovery is high. As R and Pe increase, first a single splitting evolves, to be followed by a vigorous instability involving more and more fingers at even larger values. Strong nonlinear interactions between the fingers are observed, such as merging, partial merging, and shielding, along with secondary tip-splitting and side-branching instabilities. At large Pe-values, several of these fingers compete for long times, before usually one of them accelerates ahead of the others and leads to the breakthrough of the front.

For moderate to high values of Pe, we find that the linear growth of the viscous fingering instability during early stages of the flow is predicted accurately by the linear stability analyses of Tan & Homsy (1987) and Yortsos (1987), both with regard to the algebraic growth rate, and to the preferred wavenumber. In the direct numerical simulations, the small deviations in the vicinity of the injection well between the quarter five-spot configuration and the radially symmetric source flow suffice to trigger the growth of the instability. No externally prescribed perturbations, such as the artificial permeability inhomogeneities employed in earlier investigations, are needed.

An important distinction of the quarter five-spot flow, as compared to the radially symmetric base flow, concerns the strong non-uniformity of the underlying potential base flow, with nearly radially symmetric regions of large velocities near the injection and production wells separated by the central region, in which the flow is closer to parallel, and also relatively slow. At large Pe-values, this spatial non-uniformity leads to the generation of very small scales near the injection well at early times. However, these small scales are soon convected to regions of smaller velocities, where they grow due to nonlinear mechanisms and diffusion. Only during the final stages, as the front approaches the production well, does a renewed generation of small scales occur.

Taken together, the results of the $R = $ const. and the $Pe = $ const. simulations demonstrate that both of these dimensionless quantities strongly affect the dynamics

of the flow. While some integral measures, such as the recovery at breakthrough, may show only a weak dependence on Pe for large Pe-values, the local fingering dynamics continue to change with Pe. Understanding these changes represents an important prerequisite for designing strategies to increase the overall efficiency of the displacement process. The observation that the dynamical fingering behaviour cannot be predicted on the basis of R alone, as has often been attempted in the past, is in complete agreement with earlier linear stability analyses for different base flows, which demonstrate the importance of the dimensionless flow rate Pe (Tan & Homsy 1986, 1987; Rogerson & Meiburg 1993*a*). It suggests that any predictive reservoir models will have to properly account for its influence.

The distinct flow regimes observed for different values of the governing parameters have a strong effect on such integral quantities as breakthrough time and recovery. In general, larger Pe-values and mobility ratios lower the overall recovery. However, several plateau-like regimes can appear in this functional relationship, separated by transitional regions that are characterized by changes in the overall flow dynamics, such as the onset of fingering, the evolution of secondary instabilities, etc.

The early experiments by Habermann (1960) explore the recovery at breakthrough as a function of the mobility ratio. The author reports no significant effect of the flow rate on the sweep efficiency at breakthrough; however, he does not mention the range over which he varied the flow rate. Figure 20 shows Habermann's results regarding the recovery at breakthrough (one set of data is based on the volume of injected fluid, the other on the area contacted), along with our computational results for different values of Pe and R. Overall, the agreement improves for those simulations with higher Pe-values. Again, it needs to be kept in mind that the present investigation accounts for molecular diffusion only, while neglecting the effects of velocity-dependent dispersion. In the experiments, the Pe-value might vary only weakly with the flow rate. Also plotted are the recent measurements by Zhang *et al.* (1997), which agree well with Habermann's volume-based data. Lacey *et al.* (1961) present experimental data for the mobility ratios of 1, 10, and 41, and for a large range of flow rates. Unfortunately, the authors do not provide enough information for us to calculate a Péclet number. Nevertheless, their experiments display a weak, but noticeable tendency towards lower recovery for higher flow rates, in agreement with our computational results. The data are reproduced in figure 20 as well.

An interesting observation that deserves to be explored in more detail concerns the possibility of optimizing the breakthrough recovery by employing a time-dependent flow rate. The present simulations show that initially low flow rates can partially stabilize the flow, thereby preventing the excessive early generation of small scales. During the later flow stages, when the increasing alignment of the front with the flow results in its shear stabilization, larger flow rates can be employed at a lower penalty in terms of reduced efficiency. Consequently, within the present framework which accounted for molecular diffusion only, for a constant overall process time, a time-dependent injection rate has the potential of enhancing the breakthrough recovery.

It is now of interest to employ the detailed information provided by the above simulations in order to characterize the *global* features of the displacement process. For unstable rectilinear displacements, this is typically done by analysing the temporal evolution of the mixing length l_{mix}, which tracks the distance between the 0.1 and 0.9 contours of the spanwise-averaged concentration profile. It is well established that, for small initial perturbations, the early stages are dominated by diffusion or dispersion, respectively, so that l_{mix} grows proportionally to $t^{1/2}$. Once finite-amplitude fingers

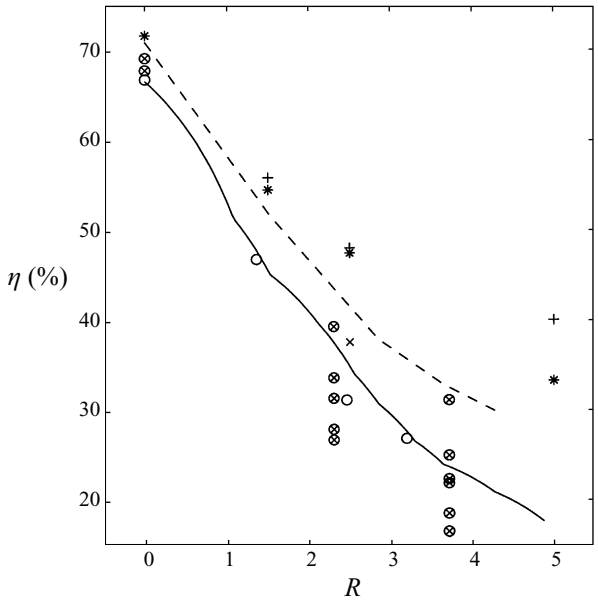

FIGURE 20. Recovery at breakthrough as function of the mobility ratio R, and for different dimensionless flow rates Pe. Solid line: volume-based data by Habermann (1960); dashed line: area-based data by Habermann (1960); ⊗, Lacey *et al.* (1961); ○, experiments by Zhang *et al.* (1997); +, present calculations, $Pe = 200$; $*$ present calculations, $Pe = 400$; × present calculations, $Pe = 2000$.

appear, the evolution of l_{mix} becomes increasingly dominated by convective effects, and its average growth is approximately proportional to t (Koval 1963; Perkins *et al.* 1965; Todd & Longstaff 1972; Tan & Homsy 1988; Araktingi & Orr 1988; Sorbie *et al.* 1992; Waggoner, Castillo & Lake 1992; Lenormand 1995). It is not obvious how an equivalent mixing length can be defined for quarter five-spot flows. Averaging over the azimuthal direction would be appropriate for radially symmetric source flows, but not for the present spatially varying base flow. Even taking the average along equipotential lines of the constant mobility irrotational flow does not give a meaningful quantity, due to the mobility-ratio dependence of the base flow. In the following, we will attempt to provide a global characterization of quarter five-spot flows in terms of the *mixing area*, defined as the area between the 0.1 and 0.9 contours. By dividing this mixing area by the instantaneous perimeter of an equivalent circular area of injected fluid, we then obtain a mixing length whose temporal evolution can be tracked. However, it needs to be kept in mind that this mixing length is still not strictly comparable to the one commonly employed in rectilinear displacements. For example, in the limit of vanishing diffusion, the front thickness will tend to zero, and according to our definition, the mixing length will vanish as well, in spite of the presence of vigorous fingering. The rectilinear mixing length definition, on the other hand, will result in a finite value, due to the averaging process it is based on.

Figure 21 depicts the development of l_{mix} with time for $R = 2.5$, with Pe as a parameter. During the initial stages and for lower Pe-values, when the nearly radially symmetric displacement is dominated by diffusion, the self-similar solution of the base flow concentration profile indicates that the front thickness grows proportionally to $t^{1/2}$. Since the perimeter of the injected area grows approximately like $t^{1/2}$ as well (cf. figure 10), the overall mixing area exhibits growth proportional to t. The mixing

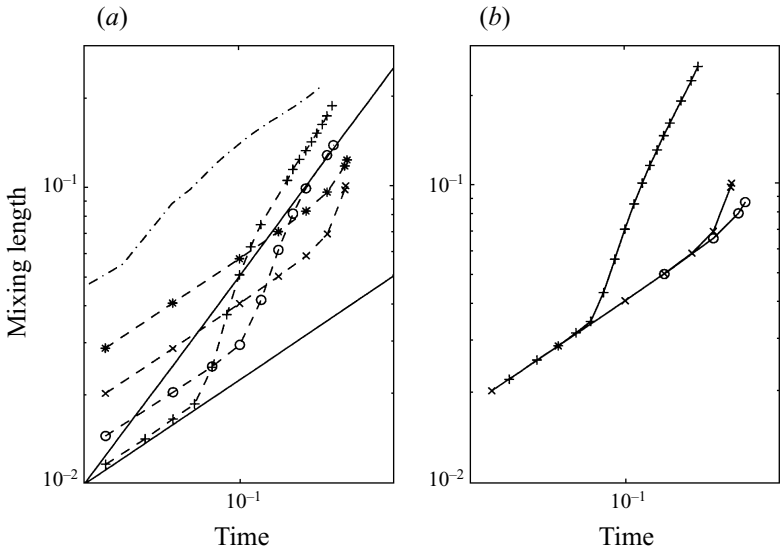

FIGURE 21. The temporal evolution of the mixing length. (*a*) As a function of Pe, for $R = 2.5$: -∗-, $Pe = 200$; -×-, $Pe = 400$; -○-, $Pe = 800$; -+-, $Pe = 1200$; ·····, $Pe = 2000$. The two solid lines have slopes of 0.5 and 1. (*b*) As a function of R, for $Pe = 400$: ○, $R = 1.5$; ×, $R = 2.5$; +, $R = 5$.

length, calculated along the lines described above, then is characterized by growth proportional to $t^{1/2}$. The smaller l_{mix} values observed for larger Pe-values and constant t_i reflect the diminished importance of diffusion.

As the initially small perturbations grow to finite amplitudes, the diffusion-dominated early stage gives way to a second phase characterized by significantly faster growth of l_{mix}. Due to the larger instability growth rates, this transition occurs at earlier times for higher Pe-values. Figure 21(*a*) shows that during this second stage, the mixing length grows at rates up to t^2. For the Pe-values of 800 and 1200, eventually a third phase is observed, during which the mixing length grows approximately linearly with time. Surprisingly, the $Pe = 2000$ simulation shows a different behaviour again, with growth proportional to $t^{1/2}$ during most of the displacement.

In order to obtain a physical interpretation of the observed growth characteristics, figure 22 compares the evolution of the mixed area over short time intervals for $Pe = 1200$ and the three distinct stages identified above. Figure 22(*a*) compares the mixing areas at times 0.0375 and 0.05. Depicted in white are additions to the mixing area during this time interval, while black indicates areas that were mixed at the earlier time but not at the later one. The figure confirms the nearly radially symmetric evolution of the mixing area, which during this early phase is dominated by diffusion. Figure 22(*b*) compares times 0.1 and 0.1125. This second phase is characterized by the active and nonlinear evolution of fingers along nearly the entire circumference, resulting in vigorous growth of the mixing area. Finally, figure 22(*c*) compares times 0.25 and 0.2634. During this late stage, large sections of the front have become more or less passive. They show almost no advance at all any more, and the mixing area in these sections grows very slowly and entirely due to diffusion. The central region, on the other hand, is characterized by very active fingers, whose length grows rapidly due to convective effects. The fingering dynamics in this central front section resembles that observed in rectilinear displacements, with several fingers of comparable length competing. In this light, the finding

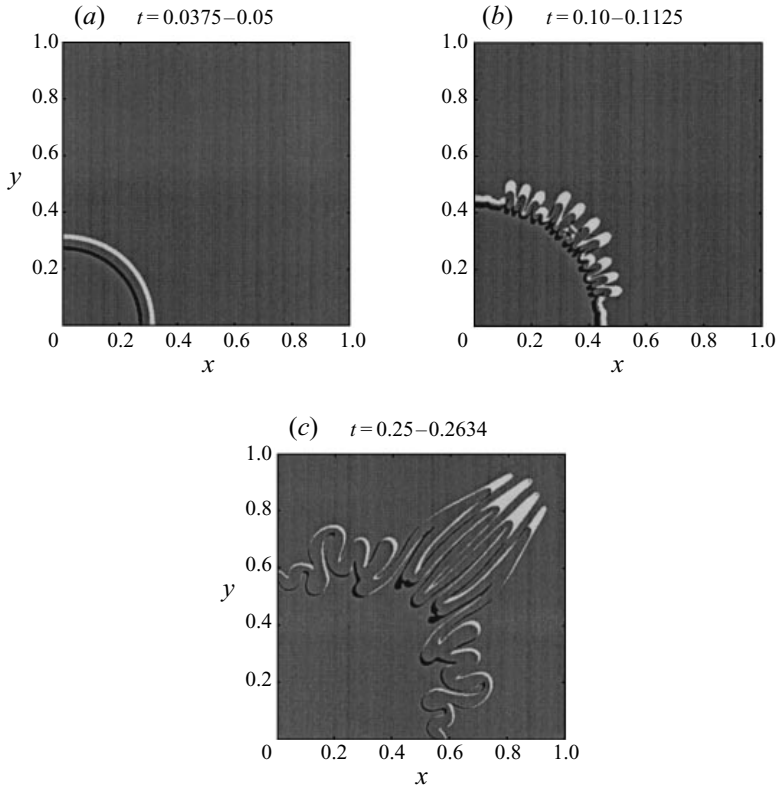

FIGURE 22. $R = 2.5, Pe = 1200$. Changes in the mixing area over small time intervals. Light regions indicate additions to the mixing area, while dark regions mark mixing area losses.

of a mixing length growth rate similar to that observed in rectilinear flows is not surprising.

The $t^{1/2}$ growth exhibited by the $Pe = 2000$ simulation indicates a nearly self-similar *convective* growth, as opposed to the early self-similar *diffusive* growth. This trend toward self-similar growth is supported by figure 23, which shows the $c = 0.5$ concentration contour at different times, with the coordinate axes rescaled by $t^{1/2}$. The figure indicates the tendency of large sections of the front to remain centred around constant rescaled spatial coordinates.

Figure 21(*b*) shows the evolution of the l_{mix} for $Pe = 400$, with R serving as parameter. While the displacements for $R = 1.5$ and 2.5 never fully reach the state where l_{mix} grows proportionally to time, the $R = 5$ case shows a very long and pronounced region of faster than linear growth, similar to the intermediate phases described for figure 21(*a*).

The above analysis shows that, in many ways, the governing mechanisms can be analysed more easily in terms of the dynamical evolution of the underlying vorticity field, an observation that goes back to de Josselin de Jong (1960). By interpreting vorticity as a 'source' of the perturbation velocity field, the acceleration of the front towards the production well as a result of an unfavourable mobility contrast becomes obvious. The vorticity generated as a result of the mobility variations leads to a dipole-like global perturbation velocity field, which augments the base flow along the diagonal, while retarding it near the edges of the domain. For large Pe-values, smaller

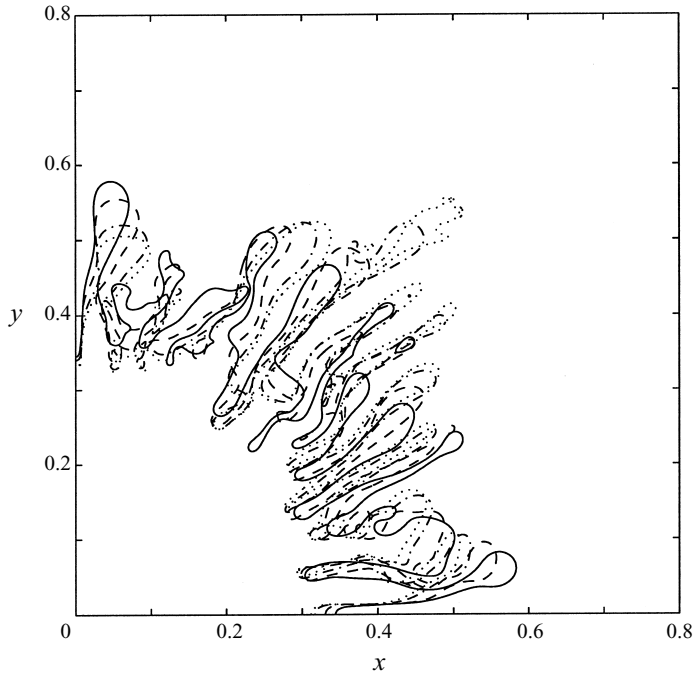

FIGURE 23. $R = 2.5, Pe = 1200$. The $c = 0.5$ concentration contour at different times, with all lengths rescaled by $t^{1/2}$. Large sections of the front show a tendency toward a self-similar evolution. —, $t = 0.10$; - - -, $t = 0.15$; -·-·-, $t = 0.20$; · · · ·, $t = 0.22$.

scales are superimposed on this global dipole structure, which favour the growth of individual fingers, even along the boundaries.

The analysis of the displacement process in terms of the underlying vorticity field also offers advantages when it comes to extending the above simulations to heterogeneous porous media. As can be seen from the vorticity equation, permeability heterogeneities lead to the existence of additional vorticity in the flow field, so that one can interprete the dynamical evolution as a being caused by a 'viscosity vorticity mode' and a 'permeability vorticity mode,' as well as the interaction between the two. The preliminary numerical investigation by Tan & Homsy (1992), as well as the work by De Wit & Homsy (1997*a,b*), indicate the possibility for a strong coupling between the two modes which can even display resonance-like phenomena. These issues will be addressed in more detail in Part 2 of the present investigation (Chen & Meiburg 1998). It should be mentioned that the presence of gravity in a fully three-dimensional displacement with density differences provides a third source of vorticity, with possibilities for even more complex interactions.

We would like to acknowledge several stimulating discussions with Yanis Yortsos, Tony Maxworthy, Philippe Petitjeans, and Hamdi Tchelepi. We furthermore thank Professor Yortsos for bringing several of the references to our attention. Partial support by a NATO Collaborative Research Grant, by the National Science Foundation in form of an equipment grant, and by the Chevron Petroleum Technology Company is gratefully acknowledged. We furthermore thank the NSF sponsored San Diego Supercomputer Centre for providing computing time.

REFERENCES

Adler, P. M. & Brenner, H. 1988 Multiphase flow in porous media. *Ann. Rev. Fluid Mech.* **20**, 35.

Araktingi, U. G. & Orr Jr., F. M. 1988 Viscous fingering in heterogeneous porous media. *SPE Paper* 18095.

Bacri, J.-C., Rakotomalala, N., Salin, D. & Woumeni, R. 1992 Miscible viscous fingering: Experiments versus continuum approach. *Phys. Fluids* A **4**, 1611.

Batycky, R. P., Blunt, M. J. & Thiele, M. R. 1996 A 3D field scale streamline simulator with gravity and changing well conditions. *SPE Paper* 36726.

Blackwell, R. J., Rayne, J. R. & Terry, W. M. 1959 Factors influencing the efficiency of miscible displacement. *Trans. AIME* **216**, 1.

Brand, C. W., Heinemann, J. E. & Aziz, K. 1991 The grid orientation effect in reservoir simulation. *SPE Paper* 21228.

Bratvedt, F., Bratvedt, K., Buchholz, C. F., Holden, L., Holden, H. & Risebro, N. H. 1992 A new front-tracking method for reservoir simulation. *SPE Res. Engng* (Feb. 1992), 107.

Brock, D. C. 1990 An experimental investigation of viscous fingering in heterogeneous porous medua. PhD dissertation, Stanford University.

Caudle, B. H. & Witte, M. D. 1959 Production potential changes during sweep-out in a five-spot system. *Trans. AIME* **216**, 446.

Chen, C.-Y. 1998 Topics in miscible porous media flows. PhD dissertation, University of Southern California, Los Angeles.

Chen, C.-Y. & Meiburg, E. 1996 Miscible displacement in capillary tubes. Part 2. Numerical simulations. *J. Fluid Mech.* **326**, 57.

Chen, C.-Y. & Meiburg, E. 1998 Miscible porous media displacements in the quarter five-spot configuration. Part 2. Effect of heterogeneities. *J. Fluid Mech.* **371**, 269.

Chouke, R.L., Meurs, P. van & Poel, C. van der 1959 The instability of slow, immiscible, viscous liquid-liquid displacements in permeable media. *Trans. AIME* **216**, 188.

Christie, M. A. 1989 High-resolution simulation of unstable flows in porous media. *SPE Res. Engng* (Aug. 1989), 297.

Christie, M. A. & Bond, D. J. 1985 Multidimensional flux corrected transport for reservoir simulation. *SPE Paper* 13505.

Christie, M. A. & Bond, D. J. 1987 Detailed simulation of unstable processes in miscible flooding. *SPE Res. Engng* (Nov. 1987), 514.

Degregoria, A. J. 1985 A predictive Monte Carlo simulation of two-fluid flow through porous media at finite mobility ratio. *Phys. Fluids* **28**, 2933.

De Wit, A. & Homsy, G. M. 1997*a* Viscous fingering in periodically heterogeneous porous media. I: Formulation and linear instability. *J. Chem. Phys.* **107**, 9609.

De Wit, A. & Homsy, G .M. 1997*b* Viscous fingering in periodically heterogeneous porous media. II: Numerical simulations. *J. Chem. Phys.* **107**, 9619.

Ewing, R. E., Russel, T. F. & Young, L. C. 1989 An anisotropic coarse-grid dispersion model of heterogeneity and viscous fingering in five-spot miscible displacement that matches experiments and fine-grid simulations. *SPE Paper* 18441.

Fayers, F. J., Blunt, M. J. & Christie, M. A. 1992 Comparisons of empirical viscous fingering models and their calibration for heterogeneous problems. *SPE Res. Engng* (May 1992), 195.

Gottlieb, D. & Orszag, S. A. 1977 *Numerical Analysis of Spectral Methods: Theory and Applications.* SIAM.

Habermann, B. 1960 The efficiency of miscible displacement as a function of mobility ratio. *Trans. AIME* **219**, 264.

Hatziavramidis, D. T. 1990 A new computational approach to the miscible displacement problem. *SPE Res. Engng* (November 1990), 631.

Hill, S. 1952 Channeling in packed columns. *Chem. Engng Sci.* **1**, 247.

Homsy, G. M. 1987 Viscous fingering in porous media. *Ann. Rev. Fluid Mech.* **19**, 271.

Josselin de Jong, G. de 1960 Singularity distributions for the analysis of multiple-fluid flow through porous media. *J. Geophys. Res.* **6**5, 3739.

King, M. J. & Scher, H. 1985 Probabilistic stability analysis of multiphase flow in porous media. *SPE Paper* 14366.

Koch, D. L. & Brady, J. F. 1987 A non-local description of advection-diffusion with application to dispersion in porous media. *J. Fluid Mech.* **180**, 387.

Koch, D. L. & Brady, J. F. 1988 Anomalous diffusion in heterogeneous porous media. *Phys. Fluids* **31**, 965.

Koval, E. J. 1963 A method for predicting the performance of unstable miscible displacement in heterogeneous media. *Soc. Petrol. Engrs J.* **3**, 145.

Lacey, J. W., Faris, J. E. & Brinkman, F. H. 1961 Effect of bank size on oil recovery in the high-pressure gas-driven LPG-bank process. *Trans. AIME* **222**, 806.

Lamb, H. 1932 *Hydrodynamics*. Dover.

Lele, S. K. 1992 Compact finite difference schemes with spectral-like resolution. *J. Comput. Phys.* **103**, 16.

Lenormand, R. 1995 Transport equations for fluid displacements in stratified porous media. *SPE Paper* 30797.

Meiburg, E. & Chen, C.-Y. 1997 A high-accuracy implicit finite difference algorithm for direct numerical simulations of miscible porous media flows. *J. Comput. Phys.* (submitted).

Meiburg, E. & Homsy, G. M. 1988 Nonlinear unstable viscous fingers in Hele-Shaw flows. II. Numerical simulation. *Phys. Fluids* **31**, 429.

Morel-Seytoux, H. J. 1965 Analytical-numerical method in waterflooding predictions. *Soc. Petrol. Engrs J.* (Sept. 1965), 247.

Morel-Seytoux, H. J. 1966 Unit mobility ratio displacement calculations for pattern floods in homogeneous medium. *Soc. Petrol. Engrs J.* (Sept. 1966), 217.

Muskat, M. 1937 *The Flow of Homogeneous Fluids through Porous Media*. McGraw-Hill.

Pankiewitz, C. & Meiburg, E. 1998 Miscible porous media displacements in the quarter five-spot configuration. Part 3. Non-monotonic viscosity profiles. *J. Fluid Mech.* (submitted).

Paterson, L. 1984 Diffusion-limited aggregation and two-fluid displacements in porous media. *Phys. Rev. Lett.* **52**, 1621.

Peaceman, D. W. & Rachford, H. H. 1955 The numerical solution of parabolic and elliptic differential equations. *SIAM J.* **3**, 28.

Peaceman, D. W. & Rachford, H. H. 1962 Numerical calculation of multidimensional miscible displacement. *Soc. Petrol. Engrs J.* (Dec. 1962), 327.

Perkins, T. K., Johnston, O. C. & Hoffman, R. N. 1965 Mechanics of viscous fingering in miscible systems. *Soc. Petrol. Engrs J.* **5**, 301.

Petitjeans, P. & Maxworthy, T. 1996 Miscible displacement in capillary tubes. Part 1. Experiments. *J. Fluid Mech.* **326**, 37.

Rogerson, A. & Meiburg, E. 1993*a* Shear stabilization of miscible displacement processes in porous media. *Phys. Fluids* A **5**, 1344.

Rogerson, A. & Meiburg, E. 1993*b* Numerical simulation of miscible displacement processes in porous media flows under gravity. *Phys. Fluids* A **5**, 2644.

Saffman, P. G. 1986 Viscous fingering in Hele-Shaw cells. *J. Fluid Mech.* **173**, 73.

Saffman, P. G. & Taylor, G. I. 1958 The penetration of a fluid into a porous medium or Hele-Shaw cell containing a more viscous liquid. *Proc. R. Soc. Lond.* A **245**, 312.

Sherwood, J. D. 1987 Unstable fronts in a porous medium. *J. Comput. Phys.* **68**, 485.

Simmons, J., Landrum, B. L., Pinson, J. M. & Crawford, P.B. 1959 Swept areas after brekthrough in vertically fractured five-spot patterns. *Trans. AIME* **216**, 73.

Slobod, R. L. & Thomas, R. A. 1963 Effect of transverse diffusion on fingering in miscible-phase displacement. *Soc. Petrol. Engrs J.* **3**, 9.

Sorbie, K. S., Feghi, F., Pickup, G. E., Ringrose, P. S. & Jensen, J. L. 1992 Flow regimes in miscible displacements in heterogeneous correlated random fields. *SPE Paper* 24140.

Tan, C. T. & Homsy, G. M. 1986 Stability of miscible displacements in porous media: Rectilinear flow. *Phys. Fluids* **29**, 3549.

Tan, C. T. & Homsy, G. M. 1987 Stability of miscible displacements in porous media: Radial source flow. *Phys. Fluids* **30**, 1239.

Tan, C. T. & Homsy, G. M. 1988 Simulation of nonlinear viscous fingering in miscible displacement. *Phys. Fluids* **31**, 1330.

Tan, C. T. & Homsy, G. M. 1992 Viscous fingering with permeability heterogeneity. *Phys. Fluids* A **4**, 1099.

Taylor, G. I. 1953 Dispersion of soluble matter in solvent flowing slowly through a tube. *Proc. R. Soc. Lond.* A **219**, 186.

Tchelepi, H. A. & Orr, F. M. Jr. 1994 Interaction of viscous fingering, permeability inhomogeneity, and gravity segregation in three dimensions. *SPE Res. Engng* (November 1994), 266.

Tchelepi, H. A., Orr, F. M. Jr., Rakotomalala, N., Salin, D. & Woumeni, R. 1993 Dispersion, permeability heterogeneity, and viscous fingering: Acoustic experimental observations and particle-tracking simulations. *Phys. Fluids* A **5**, 1558.

Thiele, M. R., Batycky, R. P., Blunt, M. J. & Orr, F. M. 1996 Simulating flow in heterogeneous media using streamtubes and streamlines. *SPE Reservoir Engng* **10** (1), 5.

Todd, M. R. & Longstaff, W. J. 1972 The development, testing and application of a numerical simulator for predicting miscible flood performance. *Soc. Petrol. Engrs J.* **12**, 874.

Tryggvason, G. & Aref, H. 1983 Numerical experiments on Hele-Shaw flow with a sharp interface. *J. Fluid Mech.* **136**, 1.

Waggoner, J. R., Castillo, J. L. & Lake, L. W. 1992 Simulation of EOR processes in stochastically generated permeable media. *Soc. Petrol. Engrs Form. Eval.* (June 1992), 173.

Wooding, R. A. 1969 Growth of fingers at an unstable diffusing interface in a porous medium or Hele-Shaw cell. *J. Fluid Mech.* **39**, 477.

Wooding, R. A. & Morel-Seytoux, H. J. 1976 Multiphase fluid flow through porous media. *Ann. Rev. Fluid Mech.* **8**, 233.

Yang, Z. & Yortsos, Y. C. 1997 Asymptotic solutions of miscible displacements in geometries of large aspect ratio. *Phys. Fluids* **9**, 286.

Yortsos, Y. C. 1987 Stability of displacement processes in porous media in radial flow geometeries. *Phys. Fluids* **30**, 2928.

Yortsos, Y. C. 1990 Instabilities in displacement processes in porous media. *J. Phys.: Condens. Matter* **2**, SA 443.

Yortsos, Y. C. & Zeybek, M. 1988 Dispersion driven instability in miscible displacement in porous media. *Phys. Fluids* **31**, 3511.

Zhang, H. R., Sorbie, K. S. & Tsibuklis, N. B. 1997 Viscous fingering in five-spot experimental porous media: New experimental results and numerical simulation. *Chem. Engng Sci.* **52**, 37.

Zimmerman, W. B. & Homsy, G. M. 1992 Viscous fingering in miscible displacements: Unification of effects of viscosity contrast, anisotropic dispersion, and velocity dependence of dispersion on nonlinear finger propagation. *Phys. Fluids* A **4**, 1099.